

A comprehensive exploration of quasisymmetric stellarators and their coil sets

Andrew Giuliani^{1†}, Eduardo Rodríguez² and Marina Spivak¹

¹Center for Computational Mathematics, Flatiron Institute, 162 Fifth Avenue, New York, 10128, USA

²Max Planck Institute of Plasma Physics at Greifswald, Wendelsteinstraße 1, 17491 Greifswald, Germany

(Received xx; revised xx; accepted xx)

We augment the ‘QUAsi-symmetric Stellarator Repository’ (QUASR) to include vacuum field stellarators with quasihelical symmetry using a globalized optimization workflow. The database now has almost 370,000 quasisaxisymmetry and quasihelically symmetric devices along with coil sets, optimized for a variety of aspect ratios, rotational transforms, and discrete rotational symmetries. This paper outlines a couple of ways to explore and characterize the data set. We plot devices on a near-axis quasisymmetry landscape, revealing close correspondence to this predicted landscape. We also use principal component analysis to reduce the dimensionality of the data so that it can easily be visualized in two or three dimensions. Principal component analysis also gives a mechanism to compare the new devices here to previously published ones in the literature. We are able to characterize the structure of the data, observe clusters, and visualize the progression of devices in these clusters. These techniques reveal that the data has structure, and that typically one, two or three principal components are sufficient to characterize it. The latest version of QUASR is archived at <https://zenodo.org/doi/10.5281/zenodo.10050655> and can be explored online at quasr.flatironinstitute.org.

Key words: quasisymmetry, stellarators, optimization, principal component analysis, dimensionality reduction

1. Introduction

In recent years, the stellarator community has developed novel numerical optimization algorithms to quickly design stellarators that are quasisymmetric. Quasisymmetry (QS) is a property of the magnetic field, where the field strength on a given magnetic surface can be written as a linear combination of the Boozer angles (Boozer 1981a) on the surface (Helander 2014). It can be shown that such fields confine guiding center orbits (Boozer 1981b; Nührenberg & Zille 1988; Rodriguez *et al.* 2020; Burby *et al.* 2020). Two important types of quasisymmetry that we consider in this work are quasisaxisymmetry (QA) and quasihelical symmetry (QH). Gradient-based optimization algorithms have facilitated the design of magnetic fields with the QS property (Landreman & Paul 2022), as well as the electromagnetic coils that generate them (Wechsung *et al.* 2022).

There is interest in the stellarator community to explore the landscape of QS stellarators. To this end, a data set of 500,000 stellarators optimized for near-axis quasisymmetry

† Email address for correspondence: agiuliani@flatironinstitute.org

(Garren & Boozer 1991; Landreman *et al.* 2019; Landreman & Sengupta 2019*b*) was published in Landreman (2022). A set of four stellarators with highly precise volumetric quasisymmetry was published in Landreman & Paul (2022). Using similar techniques, a data set of more than 150 devices was released in Buller *et al.* (2024). Adjoint-based algorithms were used to generate a set of over 30 quasisymmetric stellarators (Nies *et al.* 2024). The devices in the data sets mentioned above all were released without the coil sets that generate them. A data set of over 40 stellarator coil sets was compiled to study the effect of the magnetic length scale on coil placement (Kappel *et al.* 2024). A set of over 10 devices with simple and flexible coils was compiled in Jorge *et al.* (2024) using a variety of direct coil optimization algorithms.

A globalized coil design workflow was recently described in Giuliani (2024), and was used to generate a large database of quasaxisymmetric stellarators and their associated coil sets. The database is called QUASR for ‘QUAsi-symmetric Stellarator Repository’ and can be explored online at quasr.flatironinstitute.org. In this work, we extend these algorithms to search for quasihelically symmetric devices and augment QUASR so that it now contains around 370,000 devices with associated coil sets. Using this large data set, we explore the landscape of stellarators that are generated by modular electromagnetic coils. To start, we present a few devices in QUASR and analyze their physics properties. We then apply a variety of techniques to visualize and analyze this large data set. The first uses near-axis arguments to generate a landscape that reveals areas of parameter space with excellent and poor quasisymmetry (Rodríguez *et al.* 2022*b*; Rodríguez *et al.* 2023), which we call the near-axis quasisymmetry landscape. Then, we employ a dimensionality reduction approach called principal component analysis (PCA) (Jolliffe 1990). This is a well-known technique frequently used in data science for dimensionality reduction and visualization (Bishop 2006). It enables the practitioner to project the high-dimensional data set onto a linear manifold, e.g., a two-dimensional plane or three-dimensional volume, to visualize relationships and possible formation of clusters. We compute two quantitative scores that measure how faithful the lower-dimensional representation is to the higher-dimensional data.

To summarize, the main goals of this paper are twofold: (1) we extend QUASR to include both QA and QH stellarators (Sections 2, 3), and (2) we use a couple of visualization techniques to explore the data set and gain insight on the devices in it (Sections 4, 5).

2. The coil design workflow

Our goal is to find coil geometries and currents that produce magnetic fields with the QS property (either QA or QH). To achieve this, we use a globalized coil design workflow that comprises three phases, wrapped in a globalization algorithm. Since this workflow and its constituent algorithms have been described before (Eriksson *et al.* 2019; Giuliani 2024; Giuliani *et al.* 2022*a*, 2023, 2022*b*), we only provide a brief overview here, summarized in Figure 1. The first phase searches for stellarator coils that have near-axis quasisymmetry. This algorithm is robust, but may only find devices with nested flux surfaces on a small region in the neighborhood of the magnetic axis. These devices are then provided as an initial guess to the final two phases which heal generalized chaos, optimize for nested flux surfaces, and polish for precise quasisymmetry. The three phases are wrapped in a globalization algorithm (Eriksson *et al.* 2019), ensuring that the objective landscape is sufficiently well-explored.

There are two flavors of quasisymmetry that we are interested in: quasaxisymmetry and quasi-helical symmetry. The approach to optimize coils for both symmetries are very

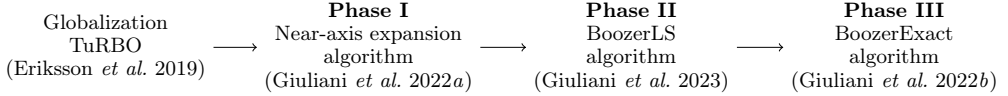
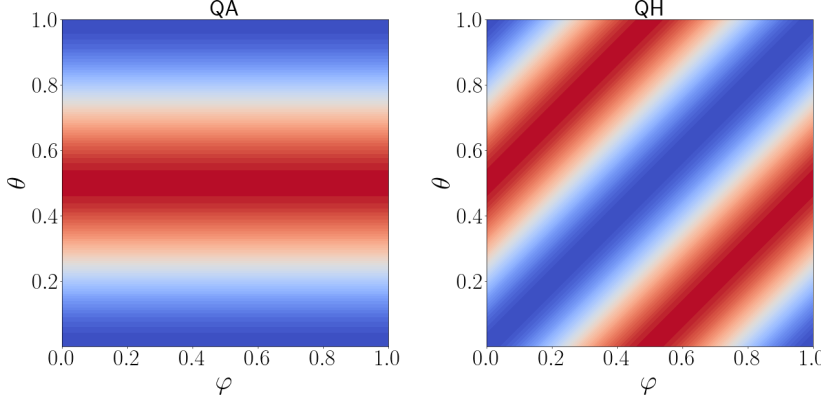


FIGURE 1. Globalized coil design workflow.

FIGURE 2. $B(\varphi, \theta)$ for quasisymmetry and quasi-helical symmetry. φ and θ are Boozer angles, where the toroidal angle is normalized by $2\pi/n_{fp}$, and the poloidal angle is normalized by 2π .

similar, so we explain first the process for quasisymmetry then explain how it can be extended to quasi-helical symmetry. quasisymmetry is characterized by horizontal isolines of $B(\varphi, \theta) = \|\mathbf{B}(\Sigma_s(\varphi, \theta))\|$, on magnetic flux surfaces Σ_s parametrized in Boozer coordinates (φ, θ) (Boozer 1981a), shown in Figure 2. The field's deviation from exact quasisymmetry on the magnetic surface can be computed by evaluating:

$$\frac{\int_0^{1/n_{fp}} \int_0^1 (B(\varphi, \theta) - B_{QA}(\theta))^2 \left\| \frac{\partial \Sigma_s}{\partial \varphi} \times \frac{\partial \Sigma_s}{\partial \theta} \right\| d\theta d\varphi}{\int_0^{1/n_{fp}} \int_0^1 B_{QA}(\varphi, \theta)^2 \left\| \frac{\partial \Sigma_s}{\partial \varphi} \times \frac{\partial \Sigma_s}{\partial \theta} \right\| d\theta d\varphi}, \quad (2.1)$$

where

$$B_{QA}(\theta) = \frac{\int_0^{1/n_{fp}} B(\varphi, \theta) \left\| \frac{\partial \Sigma_s}{\partial \varphi} \times \frac{\partial \Sigma_s}{\partial \theta} \right\| d\varphi}{\int_0^{1/n_{fp}} \left\| \frac{\partial \Sigma_s}{\partial \varphi} \times \frac{\partial \Sigma_s}{\partial \theta} \right\| d\varphi} \quad (2.2)$$

is a least squares projection of $B(\varphi, \theta)$ onto the space of functions that do not depend on φ . These integrals can easily be evaluated using the quadrature points on the tensor product grid $(\varphi_i, \theta_j) \in [0, 1/n_{fp}] \times [0, 1]$, where $\varphi_i = i/(N_\varphi n_{fp})$ and $\theta_j = j/N_\theta$ for $i = 0, \dots, N_\varphi - 1$, $j = 0, \dots, N_\theta - 1$, and N_φ, N_θ are the number of quadrature points in the toroidal and poloidal directions, respectively. These points correspond to the periodic trapezoidal rule, which is spectrally accurate (Trefethen & Weideman 2014). This measure of quasisymmetry is similar to the commonly used sum over the symmetry breaking components of B (Rodríguez et al. 2022a).

Quasihelical symmetry is characterized by isolines of $B(\varphi, \theta)$ with a slope that is an integer multiple of $\pm n_{fp}$, (Figure 2). Most devices of interest have isolines with a slope exactly equal to $\pm n_{fp}$ (Rodríguez et al. 2023). The same formulas and quadrature points used for QA can also be used in the case of QH by applying equations (2.1)-(2.2) in the rotated frame $\tilde{\varphi} = \varphi + \theta$, $\tilde{\theta} = \varphi - \theta$.

Once a device with near-axis quasisymmetry is obtained from Phase I, phases II and III

attempt to minimize the device’s volumetric deviation from quasisymmetry, i.e., minimize (2.1) in the field generated by the electromagnetic coils on several magnetic surfaces. The devices are generated by scanning over a number of physics and engineering target characteristics. In terms of physics properties, the devices all have a major radius of 1 meter, and we target various values of mean rotational transform ι , aspect ratio, and total coil length. In terms of engineering characteristics, we impose that the coils’ curvature and mean squared curvature may not exceed 5 m^{-1} and 5 m^{-2} , respectively. The coils also are designed to have uniform incremental arclength. We refer to these as *engineering constraints*. The goal of these parameter scans is to explore the space of quasisymmetric stellarators that can be generated by coil sets, and observe possible trade-offs between competing physics and engineering characteristics. Whenever ‘quality of quasisymmetry’ for a device is provided in the manuscript, it is calculated by taking the square root of the average of (2.1) on a number of surfaces of the equilibrium.

3. A few QH designs in QUASR

In this section, we present a few devices in the data set, summarized in Table 1 and plotted in Figure 3. We estimate the guiding-center (Blank 2004) losses of alpha particles in these devices by scaling them up to the ARIES-CS (Najmabadi *et al.* 2008) minor radius and spawning 5,000 alpha particles isotropically at half-radius in SIMSOPT (Landreman *et al.* 2021), then tracing until 0.2 seconds. All equilibria have favorable particle loss estimates despite deviations from QS, most likely owing to the narrow orbit widths in QH devices (Landreman & Paul 2022; Buller *et al.* 2024; Paul *et al.* 2022). Except for the two field period device, all presented devices have reasonable elongation of flux surfaces in the RZ plane. Note that this measure of shaping (especially when large) can be somewhat misleading in devices with a large helical excursion of the magnetic axis (see Section 5.2 for additional discussion on this). In such cases it is more instructive to measure the elongation in the plane perpendicular to the magnetic axis; for the $n_{\text{fp}} = 2$ device, the maximum elongation in such plane reduces to 6.85, which is still significant.[†]

The first device is a two field period QH field with a ‘crossing point’ with little space for coils, for which coils may nevertheless be found. Although it has the highest particle losses compared to the other devices presented here, the device is reminiscent of the original figure-eight stellarator design (Spitzer 1958). The $n_{\text{fp}} = 4$ device is quite similar to the Landreman-Paul precise QH configuration (Landreman & Paul 2022), but was discovered independently with coils. The $n_{\text{fp}} = 6$ device shows an example of a configuration with a high number of field periods, which are configurations that have proved challenging to find and provide a set of coils for (Landreman 2022).

A note must be made on the coils presented for these configurations here. The filamentary coils generally appear quite long, which do not make the coil sets particularly practical. However, such having such coils remains useful at least as an initial starting point for further refinement.

4. The near-axis quasisymmetry landscape

The landscape of quasisymmetry quality in terms of the coil degrees of freedom is complex and high-dimensional, which can be difficult to visualize. Using a near-axis framework, though, this landscape gains significant structure when parametrized in terms

[†] This quantity was numerically computed by fitting a near-axis model to the field (Section 4), and providing the parameters to `pyQSC` (Landreman *et al.* 2024).

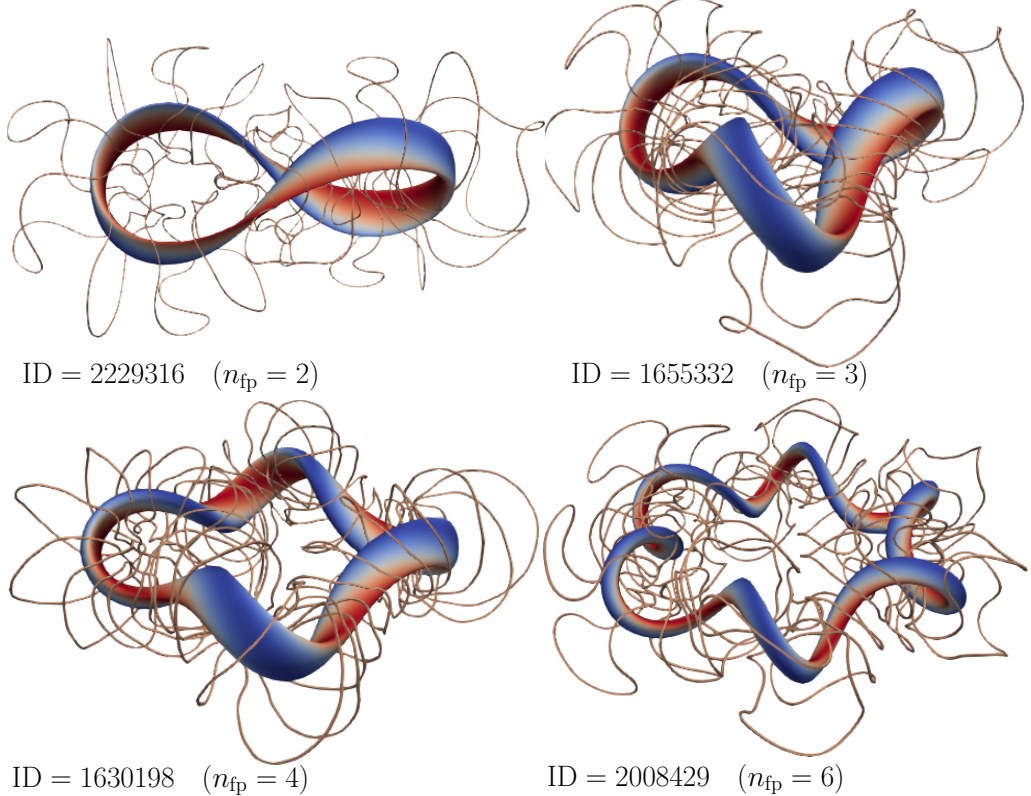


FIGURE 3. Notable QH devices and their coil sets in the QUASR.

ID	n_{fp}	mean ι	aspect ratio	max. elongation	particle losses (%)	quality of QS
2229316	2	0.9	6	8.75	3.26	4.03e-04
1655332	3	1.2	6	3.66	0.00	4.22e-04
1630198	4	1.2	8	3.62	0.00	7.54e-04
1641080	5	1.5	8	2.16	0.00	2.26e-03
2008429	6	2.5	12	2.31	0.14	8.09e-04

TABLE 1. Characteristics of some QH devices from the QUASR data set. The maximum elongation is computed in the RZ plane.

of the magnetic axis shape, owing to the key role played by topological properties of these (Rodríguez *et al.* 2022b). A representation of a representative subset of these axes described only by a few parameters (and thus lower dimensionality) can then provide a simple way to assess and visualize QS fields (Rodríguez *et al.* 2023).

To construct such a space, we start by providing the elements necessary to characterize a near-axis quasi-symmetric vacuum field (Landreman & Sengupta 2019b; Rodríguez *et al.* 2023). Such a field is defined by providing the geometry of the magnetic axis (customarily given as a set of Fourier harmonics \mathbf{R}, \mathbf{Z} describing the axis shape in cylindrical coordinates), and two scalars $\bar{\eta}$ and B_{2c} . Given such inputs, one can evaluate a function $\Delta B_{20}(\mathbf{R}, \mathbf{Z}, \bar{\eta}, B_{2c})$ which measures the magnitude of the symmetry breaking of B at second order in the distance from the magnetic axis (Landreman & Sengupta 2019b; Rodríguez *et al.* 2023). That is, if $\Delta B_{20} = 0$, then the near-axis vacuum field considered

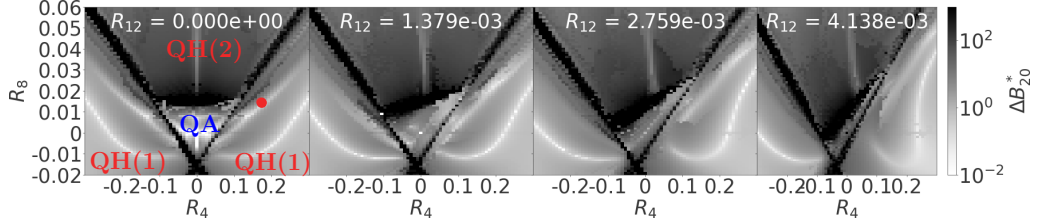


FIGURE 4. The landscape of quasisymmetric stellarators for $n_{fp} = 4$, the red dot on the leftmost panel corresponds to the HSX device. There are four quasisymmetry phases delineated by poorly quasisymmetric (dark color) devices.

has ‘perfect’ quasisymmetry to second order. This scalar function of $(\mathbf{R}, \mathbf{Z}, \bar{\eta}, B_{2c}) \in \mathbb{R}^{2N+1}$ variables is too high-dimensional for straightforward plotting. Using the approach in Rodríguez *et al.* (2023), one may nevertheless reduce this complexity to a minimum that retains the critical structure of the problem. This reduction of the space draws from the following logic:

- (i) the main structural element in the field description is the axis shape, which will remain our free parameters. For visualization purposes, the axis geometry is restricted to a few harmonics, in this case $\mathbf{R} = (1, R_{n_{fp}}, R_{2n_{fp}}, R_{3n_{fp}})$, and $\mathbf{Z} = (Z_{n_{fp}}, Z_{2n_{fp}}, Z_{3n_{fp}})$,
- (ii) for a given axis shape, $\bar{\eta} = \bar{\eta}^\dagger(\mathbf{R}, \mathbf{Z})$ is chosen uniquely to roughly minimize elongation of surfaces, formally

$$\bar{\eta}^\dagger = \operatorname{argmax}_{\bar{\eta}} |\iota(\bar{\eta}) - N|. \quad (4.1)$$

where ι is the on-axis rotational transform and N is the helicity (see Rodríguez *et al.* (2023) for further details and proofs). Changing the value of $\bar{\eta}$ will directly affect elongation of surfaces as well as the rotational transform.

- (iii) the \mathbf{Z} harmonics and B_{2c} are then optimized over to minimize ΔB_{20} .

This results in a scalar function

$$\Delta B_{20}^*(\mathbf{R}) = \min_{\mathbf{Z}, B_{2c}} \Delta B_{20}(\mathbf{R}, \mathbf{Z}, \bar{\eta}^\dagger(\mathbf{R}, \mathbf{Z}), B_{2c})$$

of only a function of 3 independent variables $(R_{n_{fp}}, R_{2n_{fp}}, R_{3n_{fp}})$, and it can easily be visualized by evaluating it on a three-dimensional tensor product grid using the pyQSC code (Landreman *et al.* 2024). The minimization problem over the Z harmonics (\mathbf{Z}) uses local optimization algorithms, where the Z harmonics provided to the optimization are initialized to have $\mathbf{Z} := \mathbf{R}$. This results in magnetic axes with Z harmonics that scale with R as the optimization algorithm does not stray far from the initial guess. The resulting plots have structure thanks to the topological properties of the magnetic axis (Rodríguez *et al.* 2022b). This landscape can be divided into phases (or regions) where either QA and QH devices are found, Figure 4, corresponding to axis shapes with different *self-linking* numbers (Rodríguez *et al.* 2022b; Moffatt & Ricca 1992; Fuller Jr 1999; Oberti & Ricca 2016). At the origin, we have the QA phase, surrounded by QH phases. As the magnitude of the third harmonic increases (and thus the axis shaping increases), the QA region shrinks; there is a limit to how much an axis can be shaped before it gains a non-zero helicity and represent a QH device. The east and west QH regions have helicity n_{fp} , and the north and south regions have helicity $2n_{fp}$. In Rodríguez *et al.* (2023), two branches of QH stellarators with favorable quasisymmetry were observed: the HSX branch, as well as a new QH branch that had not yet been explored. The HSX branch is

the one on which the HSX device lies, and the ‘new QH’ branch is the one below it (see the leftmost panel in Figure 4).

To visualize the devices in QUASR on this landscape, we fit the near-axis model to the magnetic fields generated by the coil sets. The algorithm to do this is described next.

Fitting the second-order near-axis model to the devices

Alongside the geometry of the field’s magnetic axis (which can be directly constructed from the given coils), there are three parameters that describe the second order near-axis model in vacuum: B_0 , $\bar{\eta}$ and B_{2c} . In the neighborhood of the magnetic axis, the field strength $B = \|\mathbf{B}\|$ of the near-axis model satisfies

$$B(r, \varphi, \theta) = B_0 + rB_0\bar{\eta}\cos(\theta - N\varphi) + r^2[B_{20}(\varphi) + B_{2c}\cos(2(\theta - N\varphi))] + \dots,$$

where stellarator symmetry is assumed, φ, θ are Boozer angles, and r is the radial distance off-axis. There are a multitude of methods to estimate these near-axis parameters in the field generated by the coils. For instance, one could evaluate the field strength on a three-dimensional tensor-product grid $(r_i, \varphi_j, \theta_k)$ in the neighborhood of the magnetic axis and solve for the values of $B_0, \bar{\eta}, B_{2c}, B_{20}(\varphi_j)$ in a least-squares sense. Another possibility is to fit the predicted cross-sections of the near-axis magnetic surfaces to the true ones (Landreman 2019). These techniques both have the difficulty that one must use information off axis, and the quality of the fit might be sensitive to the choice of how far off-axis one goes. In order to make the fitting procedure independent of this user-defined choice, we solve three minimization problems sequentially:

$$\begin{aligned} B_0^* &= \underset{B_0}{\operatorname{argmin}} \int_0^{2\pi} \|\mathbf{B}_{\text{coils}} - \mathbf{B}_{\text{NAE}}(B_0)\|^2 d\phi, \\ \bar{\eta}^* &= \underset{\bar{\eta}}{\operatorname{argmin}} \int_0^{2\pi} \|\nabla \mathbf{B}_{\text{coils}} - \nabla \mathbf{B}_{\text{NAE}}(B_0^*, \bar{\eta})\|^2 d\phi, \\ B_{2c}^* &= \underset{B_{2c}}{\operatorname{argmin}} \int_0^{2\pi} \|\nabla \nabla \mathbf{B}_{\text{coils}} - \nabla \nabla \mathbf{B}_{\text{NAE}}(B_0^*, \bar{\eta}^*, B_{2c})\|^2 d\phi, \end{aligned} \quad (4.2)$$

where ϕ is the standard cylindrical angle. Since the magnetic field is generated by a set of coils, we can compute the magnetic field as well as its first and second derivatives using the Biot-Savart law, which we have direct access to in SIMSOPT. As a result, we can find the near-axis parameters that most closely reproduce the coils’ magnetic field and its derivatives on axis. Note that the near-axis model assumes that there is perfect quasisymmetry to first order. While a good approximation of quasisymmetry is attainable in the volume, the devices do not present perfect near-axis quasisymmetry, and we may not always be able to obtain a good fit of the coils’ magnetic field.

In Figure 5, we provide a Poincaré plot alongside cross sections of surfaces generated by a first and second order near-axis expansion. The NAE model was fit using the method described in this section, revealing that the second order NAE is capable of describing the magnetic surfaces in the neighborhood of the magnetic axis much more faithfully than the first order one.

QUASR on the near-axis quasisymmetry phase space

Following the procedure above, QUASR devices may be approximated by near-axis fields and represented in the quasisymmetric phase-space discussed above. However, the assumptions used to generate the phase space plot in Figure 4 do not necessarily hold for the devices in QUASR.

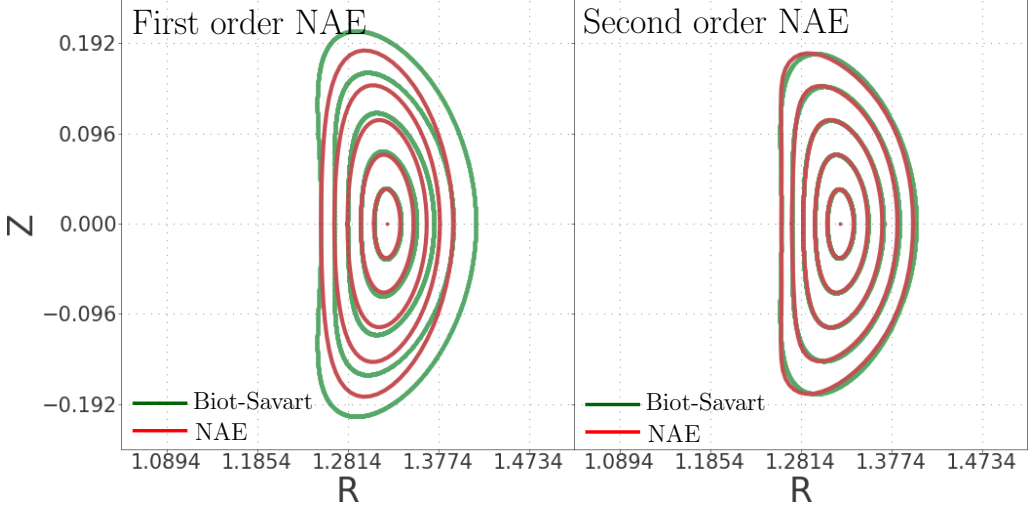


FIGURE 5. Poincaré plot (green) and cross sections of surfaces generated by the near-axis expansion (red) fit to a device in QUASR. The left panel shows the first order NAE surfaces, while the right panel shows the second order NAE surfaces. The outermost surfaces here have aspect ratio ~ 9 . The field lines are generated from starting points along the inboard side with $Z = 0$. The Biot-Savart Poincaré sections are different on the left and right panels because the field lines are initialized from different starting points.

First, note that the optimization that was used to design the devices in QUASR did not directly target the devices' elongation. As a result, we are not guaranteed that $\bar{\eta}^*$ will be close to $\bar{\eta}^\dagger$ as the phase space construction assumes. The left panel in Figure 6 shows the percentage of devices as a function of the relative error on $\bar{\eta}^*$. Around 40% of $n_{fp} = 4, 5$ devices have $|\bar{\eta}^* - \bar{\eta}^\dagger|/|\bar{\eta}^\dagger| < 0.1$ and this increases to around 70% when the upper bound is relaxed to 0.2. This illustrates that there is a non-negligible portion of devices in QUASR with possibly unrealistic elongations, which motivates the addition of constraints on surface elongation to the design workflow in Figure 1.

The right panel of Figure 6 illustrates the second of important simplifications needed to make sense of the phase space. This plot shows the fraction of devices with 1, 2, 3, etc. dominant Fourier harmonics in the description of the axis. A device is deemed to have N dominant Fourier harmonics if $R_{k,n_{fp}}(1+k^2n_{fp}^2), Z_{k,n_{fp}}(1+k^2n_{fp}^2) < 0.1$ for $k \geq N+1$.[†] Around 50% of devices have three dominant harmonics, and this number increases to around 70% when four dominant harmonics are allowed. This hints that the choice to represent magnetic axes in cylindrical coordinates and Fourier harmonics might not be the optimal choice, and an alternative parametrization of the phase space could be better suited.

With the above in mind, we plot on the phase space those devices in QUASR that satisfy:

- (i) the device's $\bar{\eta}^*$ has a relative error of at most 10% with respect to $\bar{\eta}^\dagger$, i.e., $|\bar{\eta}^* - \bar{\eta}^\dagger|/|\bar{\eta}^\dagger| < 0.1$
- (ii) the magnetic axis has only three dominant harmonics, i.e., $R_{k,n_{fp}}(1+k^2n_{fp}^2), Z_{k,n_{fp}}(1+k^2n_{fp}^2) < 0.1$ for $k \geq 4$,

where $\bar{\eta}^\dagger, \bar{\eta}^*$ are computed using the approaches described above. It is also ensured that

[†] This is a natural dimensionless quantity to measure relevance of axis harmonics introduced in Rodriguez *et al.* (2022b).

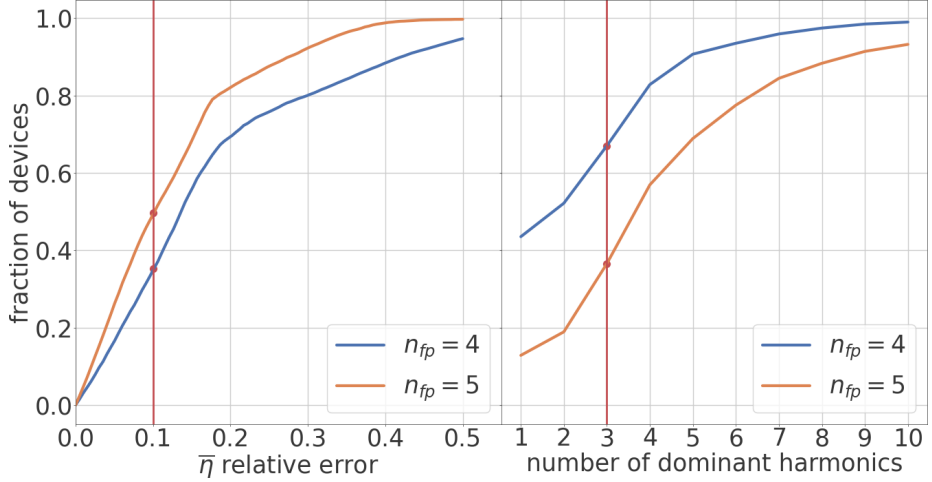


FIGURE 6. On the left panel, we show the fraction of devices that have at most some relative error between $\bar{\eta}^*$ and $\bar{\eta}^\dagger$, $|\bar{\eta}^* - \bar{\eta}^\dagger|/|\bar{\eta}^\dagger|$. On the right panel, we provide the fraction of devices in terms of the number of dominant harmonics on the magnetic axis. The vertical red line corresponds to the subset of devices plotted in Figure 7.

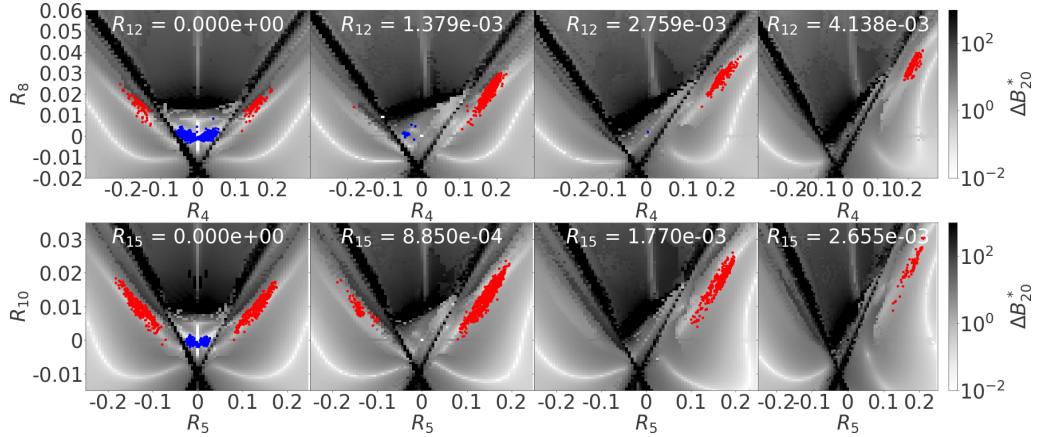


FIGURE 7. Devices optimized for QA and QH in QUASR plotted on top of the landscape with blue and red dots, respectively. The top row and bottom rows of plots correspond to $n_{fp} = 4$ and 5, respectively.

all plotted devices have $R_{3n_{fp}} > 0$. If this is not the case, then the device is rotated by a half-period, which flips the sign of the odd harmonics: $R_{n_{fp}}, R_{3n_{fp}}$. A device's coordinate on the landscape is computed from the harmonics of its magnetic axis.

The devices in QUASR optimized for QA and QH that satisfy these filters are plotted on top of Figure 4 in Figure 7. We observe that the QA devices lie as expected in the QA region. This QA region shrinks as the magnitude of the third harmonic increases, which corroborates the observation that QA devices typically do not have highly shaped magnetic axes. In the QH region, QUASR configurations appear to cluster around the HSX branch, noticeably leaving the ‘new QH’ branch, which at the time of publication the authors in Rodríguez *et al.* (2023) noted that had not yet been explored, untouched. This is so even when optimization efforts were launched directly from the new branch, cases in which optimization trajectories left the branch to find better quasisymmetry

elsewhere. Whether the struggle to find such configurations strides from the difficulty to find appropriate coils under the current engineering constraints, some intrinsic limitations on volumetric QS or the existence of a higher dimensional path in the phase space towards better QS, remains a subject of study.

While this comparison to the near-axis model is interesting and insightful, this approach has some important drawbacks. The landscape plots we obtain here are restricted to two or three dimensions before the visualizations become laborious. Despite this, it might still be possible to measure a device's distance to a favorable branch in higher dimensions, permitting some additional higher-dimensional insights. A better representation of the axes could also be fitting. In addition, the filters on $|\bar{\eta}^* - \bar{\eta}^\dagger|/|\bar{\eta}^\dagger|$ may also be unnecessarily restrictive, although as we have argued, this filter is not completely artificial if elongation of flux surfaces is taken into consideration. In the following section, we will use a different approach that applies to the entire data set.

5. Principal component analysis

Principal component analysis (PCA) is a dimensionality reduction technique that projects D -dimensional data points $\mathbf{x}_i \in \mathbb{R}^D$ onto a lower-dimensional manifold (Bishop 2006). The vector \mathbf{x}_i is also called a feature vector. For the following explanation, we focus on reducing the dimensionality of the stellarators to two-dimensional points on the plane, though one is free to retain as many dimensions as desired.

The PCA finds a plane that lies closest to the data points, and then projects the data points on this plane, thereby reducing its dimensionality. Any projected point can be expressed as $\alpha_1 \mathbf{d}_1 + \alpha_2 \mathbf{d}_2 + \gamma$, for some $\alpha_1, \alpha_2 \in \mathbb{R}$, where \mathbf{d}_1 and \mathbf{d}_2 are orthonormal. The vectors $\mathbf{d}_1, \mathbf{d}_2$ and γ are chosen to minimize the error:

$$\gamma^*, \mathbf{d}_1^*, \mathbf{d}_2^* = \underset{\substack{\gamma \text{ s.t. } \mathbf{d}_1^* \perp \mathbf{d}_2^* \\ \|\mathbf{d}_1^*\| = \|\mathbf{d}_2^*\| = 1}}{\operatorname{argmin}} \frac{1}{N} \sum_{i=1}^N \|\mathbf{x}_i - \tilde{\mathbf{x}}_i\|^2, \quad (5.1)$$

where $\tilde{\mathbf{x}}_i$ is the projection of the original point \mathbf{x}_i onto the plane of the form

$$\tilde{\mathbf{x}}_i = \gamma + \alpha_{1,i} \mathbf{d}_1 + \alpha_{2,i} \mathbf{d}_2.$$

From the orthonormality of \mathbf{d}_1 and \mathbf{d}_2 , it can be shown that $\alpha_{1,i} = \mathbf{d}_1 \cdot (\mathbf{x}_i - \gamma)$ and $\alpha_{2,i} = \mathbf{d}_2 \cdot (\mathbf{x}_i - \gamma)$, and the optimal choice of γ is the mean of the data i.e. $\gamma^* = \bar{\mathbf{x}} = \frac{1}{N} \sum_{i=1}^N \mathbf{x}_i$. The Karush-Kuhn-Tucker conditions of the minimization problem (Bishop 2006) in (5.1) reveal that the optimal choice of vectors $\mathbf{d}_1^*, \mathbf{d}_2^*$ are given by the first two eigenvectors of the covariance matrix

$$\frac{1}{N} \sum_{i=1}^N (\mathbf{x}_i - \bar{\mathbf{x}})^T (\mathbf{x}_i - \bar{\mathbf{x}}).$$

The vectors $\mathbf{d}_1^*, \mathbf{d}_2^*$ are called respectively the first and second principal components. For this choice of $\gamma^*, \mathbf{d}_1^*, \mathbf{d}_2^*$, the reconstruction error is

$$\frac{1}{N} \sum_{i=1}^N \|\mathbf{x}_i - \tilde{\mathbf{x}}_i\|^2 = \lambda_3 + \cdots + \lambda_D,$$

which is the sum of the $D - 2$ remaining eigenvalues of the covariance matrix. The ratios $\lambda_1/(\lambda_1 + \cdots + \lambda_D)$ and $\lambda_2/(\lambda_1 + \cdots + \lambda_D)$ measure by how much the first two principal components reduced the reconstruction error. If the sum of these two quantities is close

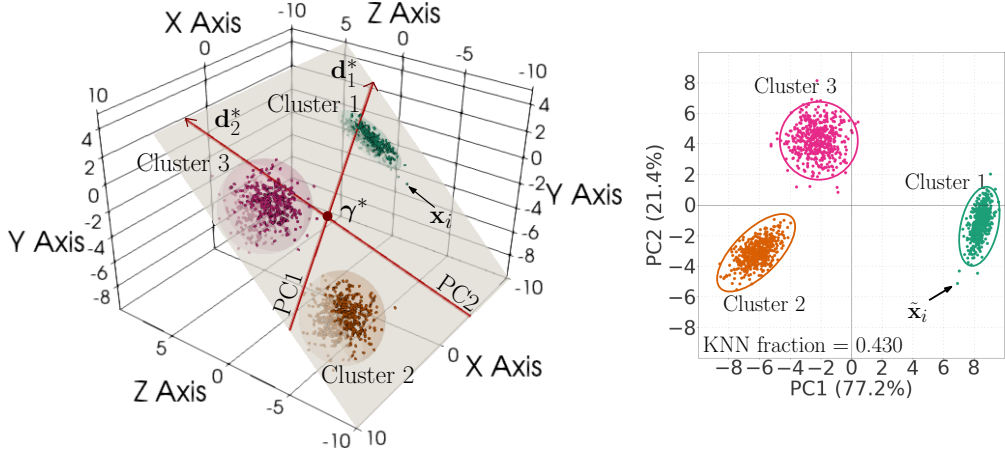


FIGURE 8. Data $\mathbf{x}_i \in \mathbb{R}^3$ from three Gaussians are shown on the left, and the optimal projection $\tilde{\mathbf{x}}_i$ onto a two-dimensional plane is shown on the right. The transparent ellipsoids correspond to the 95% confidence interval of each Gaussian.

to 1, then little information was lost in the dimensionality reduction. One is free to include as many principal components as desired, but for simplicity of plotting and ease of understanding, we restrict ourselves to two or three principal components.

Once a PCA is completed, each high-dimensional data point \mathbf{x}_i will have a corresponding two-dimensional coordinate $(\mathbf{d}_1^* \cdot (\mathbf{x}_i - \gamma^*), \mathbf{d}_2^* \cdot (\mathbf{x}_i - \gamma^*)) \in \mathbb{R}^2$. To illustrate this procedure, consider three-dimensional data points $\mathbf{x}_i \in \mathbb{R}^3$ that are projected onto a two-dimensional plane (Figure 8). Another useful property of a PCA is that projected points far away from each other on the right panel of Figure 8 will be far away from each other in the higher dimensional space. In other words, dissimilar devices in the low-dimensional representation are dissimilar in higher dimensions. Note that the converse of this statement is not necessarily true.

The advantages of PCA is that it is an unsupervised technique that does not require labels or prior knowledge about the data. It identifies important features in a low-dimensional subspace that describe the data set and permit its visualization. By doing so, it reduces the complexity and noise in the data and gives an idea of its intrinsic dimensionality, which is revealed by examining the eigenvalues of the covariance matrix. PCA is often used as a pre-processing step for machine learning and optimization algorithms to expose the most important components of the data (Kobak & Berens 2019). It also does not have any parameters to adjust, which makes it straightforward to apply to a data set.

However, PCA can also have disadvantages. By reducing the dimensionality of the data, we may lose some important information. The transformation to low-dimensional space may distort the geometric relationships that existed in the original space. In addition, PCA is useful when the data is well approximated on a linear manifold of dimension less than D , which is certainly not always the case. For example, consider a data set that lies on a three-dimensional helix. The intrinsic dimension of the data is one, since the helix can be unraveled to parameterize any point on it by a single coordinate. But applying PCA to the data set distorts it, since its topology is ill-approximated on a linear manifold of dimension less than three. In cases like this, nonlinear dimensionality reduction techniques can be useful, and the literature on these approaches is rich. For example, isomap (Tenenbaum *et al.* 2000), multidimensional scaling (Kruskal 1964), and

t-Distributed Stochastic Neighbor Embedding (Van der Maaten & Hinton 2008) are all well-known algorithms to accomplish this task. The disadvantage of nonlinear techniques is that they may have user-defined tuning parameters, which may be difficult to select. Since the underlying topology of our data set is not known, and to avoid the difficulties associated with nonlinear techniques, we use PCA in this work.

In light of the above discussion, we use a global and local measure of accuracy to evaluate how faithful the data in lower-dimensions is to the original:

- (i) *the cumulative PC ratios*: as mentioned above, this score quantifies how much information was lost in the projection onto the lower-dimensional linear manifold, corresponding to the sum of the PC ratios: $\lambda_1/(\lambda_1 + \dots + \lambda_D)$ when projecting onto a 1D manifold, $(\lambda_1 + \lambda_2)/(\lambda_1 + \dots + \lambda_D)$ when projecting onto 2D manifold, and $(\lambda_1 + \lambda_2 + \lambda_3)/(\lambda_1 + \dots + \lambda_D)$ when projecting onto a 3D manifold. The closer this value is to 1, the less information is lost in the projection. If more PCs are included, then the corresponding eigenvalues are added to the numerator. This is a global measure of accuracy.
- (ii) *KNN fraction*: the fraction of k -nearest neighbors in the high-dimensional data set that remain in the two-dimensional projected data points (Lee & Verleysen 2009; Kobak & Berens 2019), called the ‘KNN fraction’. The purpose of this quantity is to measure how accurately local relationships are preserved after dimensionality reduction. This is a local measure of accuracy.

Example: projections of Gaussians

To gain some intuition on these quality measures, we apply PCA to data generated from three Gaussians that have mean and covariance matrices:

$$\begin{aligned} \mu_1 &= \begin{pmatrix} -6 \\ 0 \\ 0 \end{pmatrix} & \Sigma_1 &= Q_1^T \begin{pmatrix} 1 & 0 & 0 \\ 0 & 10^{-1} & 0 \\ 0 & 0 & 10^{-1} \end{pmatrix} Q_1 \\ \mu_2 &= \begin{pmatrix} 6 \\ -6 \\ -6 \end{pmatrix}, & \Sigma_2 &= Q_2^T \begin{pmatrix} 1 & 0 & 0 \\ 0 & 1 & 0 \\ 0 & 0 & 10^{-1} \end{pmatrix} Q_2, \\ \mu_3 &= \begin{pmatrix} 6 \\ 0 \\ 0 \end{pmatrix}, & \Sigma_3 &= \begin{pmatrix} 1 & 0 & 0 \\ 0 & 1 & 0 \\ 0 & 0 & 1 \end{pmatrix}, \end{aligned}$$

where Q_1, Q_2 are randomly generated rotation matrices. Individually, the Gaussians are well approximated by linear manifolds of dimension one, two, and three, respectively. Samples from these distributions are shown on the left in Figure 8, while a two-dimensional projection of the data is shown on the right. In 2D, the cumulative PC ratio is quite high 0.986, revealing that the majority of variation in the data are captured by two principal components. Despite this favorable quality measure and such a simple data set, the KNN fraction is only 0.423, i.e., just over 40% of the 10 nearest neighbors in 3D remain so on the 2D projection on average.

In Figure 9, we provide the cumulative PC ratio as a function of the number of PCs. In order for the PC ratio to attain 0.9, each cluster requires a different number of PCs. This hints that cluster 1 is well approximated on a line, cluster 2 on a plane, and cluster 3 on a volume. In fact, since cluster 3 is genuinely three-dimensional, dimensionality reduction is not possible without significant loss of information. The KNN fractions increase with the number of PCs, with a value greater than 0.4 appearing to be a lower bound on a reasonable lower-dimensional representation.

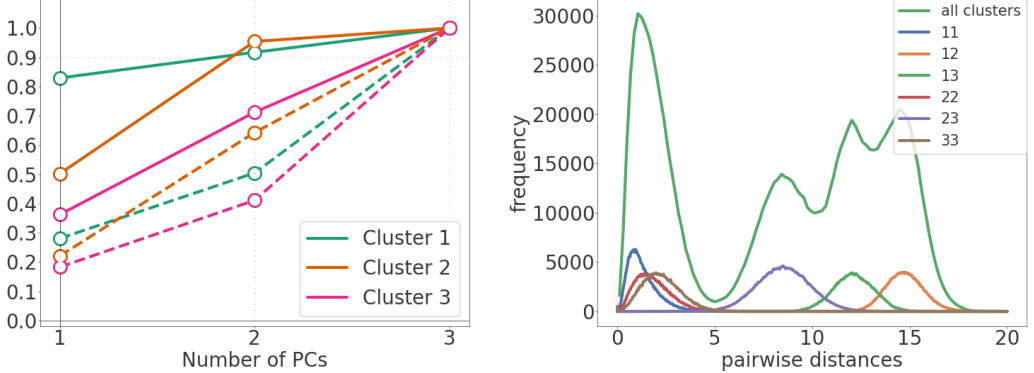


FIGURE 9. The left panel illustrates the cumulative PC ratio (solid lines) and KNN fraction (dashed lines) with respect to the number of PCs for the three clusters in Figure 8. The right panel is the histogram of pairwise distances for the same data set.

We also provide the histogram of pairwise distances, which hints to the existence of clusters in the data set. The first mode (or extremum) corresponds to pairwise distances within clusters, i.e., intra-cluster distances, while subsequent modes correspond to pairwise distances between different clusters, i.e. inter-cluster distances. Now that we have some intuition on the behavior of these quality measures applied to some simple Gaussian data, we proceed to applying PCA to the QUASR data set.

5.1. Feature vectors

In order to apply PCA to our set of stellarators, we must define how a device's feature vector is constructed. A device's feature vector containing $D = 663$ entries, where each entry is a Fourier harmonic of a stellarator symmetric surface in the device's vacuum magnetic field, using $m_{\text{pol}}, n_{\text{tor}} = 10$, where $m_{\text{pol}}, n_{\text{tor}}$ are respectively the number of poloidal and toroidal harmonics used to represent the surface geometry. We use the special surface representation (Giuliani *et al.* 2022b):

$$x(\varphi, \theta) = \cos(\varphi)\hat{x}(\varphi, \theta) - \sin(\varphi)\hat{y}(\varphi, \theta), \quad (5.2)$$

$$y(\varphi, \theta) = \sin(\varphi)\hat{x}(\varphi, \theta) + \cos(\varphi)\hat{y}(\varphi, \theta), \quad (5.3)$$

$$z(\varphi, \theta) = \sum_i \sum_j z_{i,j} u_i(\varphi) v_j(\theta), \quad (5.4)$$

where

$$\hat{x}(\varphi, \theta) = \sum_i \sum_j \hat{x}_{i,j} u_i(\varphi) v_j(\theta), \quad (5.5)$$

$$\hat{y}(\varphi, \theta) = \sum_i \sum_j \hat{y}_{i,j} u_i(\varphi) v_j(\theta), \quad (5.6)$$

and

$$\begin{aligned} u(\varphi) &= (1, \cos(2\pi n_{\text{fp}}\varphi), \sin(2\pi n_{\text{fp}}\varphi), \dots, \cos(2\pi n_{\text{fp}}n_{\text{tor}}\varphi), \sin(2\pi n_{\text{fp}}n_{\text{tor}}\varphi)) \\ v(\theta) &= (1, \cos(2\pi m_{\text{pol}}\theta), \sin(2\pi m_{\text{pol}}\theta), \dots, \cos(2\pi m_{\text{pol}}n_{\text{tor}}\theta), \sin(2\pi m_{\text{pol}}n_{\text{tor}}\theta)). \end{aligned}$$

Since we are only working with stellarator symmetric devices, the symmetry-breaking basis functions in the sums of (5.2)-(5.6) are skipped. The angles on the surface (φ, θ) correspond to Boozer coordinates. The feature vector associated to a device contains all the Fourier harmonics $\hat{x}_{i,j}, \hat{y}_{i,j}$ and $z_{i,j}$ associated to the surface.

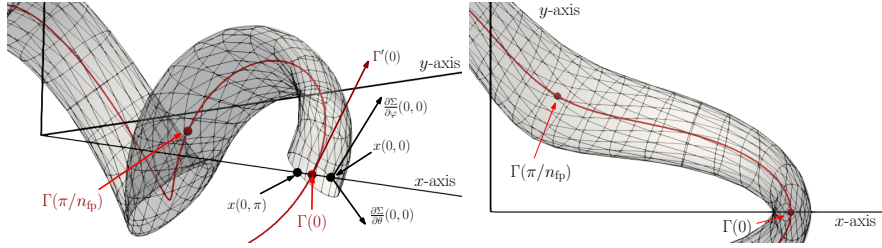


FIGURE 10. Conditions that the surface parametrization must satisfy so that the feature vector of Fourier coefficients is unique. The left image illustrates how the surface coordinates satisfy $x(0,0) \geq x(0,\pi)$, $\frac{\partial z}{\partial \theta}(0,0) \geq 0$, $\frac{\partial y}{\partial \varphi}(0,0) \geq 0$, and that the Z-coordinate of the magnetic axis (in red) satisfies $Z'(\phi) \geq 0$. The right image is a view in the $-Z$ direction onto the XY plane, showing that the radius of the magnetic axis satisfies $R(0) \geq R(\pi/n_{fp})$. The grid lines on the magnetic surface correspond to lines of constant toroidal and poloidal Boozer angles.

There is some non-uniqueness in this representation, for example a different device with the same physics properties can be obtained by a half-period rotation about the Z -axis, or reflecting the device about the XY plane. Thus, to ensure that geometrically similar devices are close to each other in Fourier space, we check that the magnetic axis in cylindrical coordinates $\Gamma(\phi) = (R(\phi), \phi, Z(\phi))$ satisfies:

1. $Z'(\phi) \geq 0$,
2. $R(0) \geq R(\pi/n_{fp})$,

and that the surface $\Sigma(\varphi, \theta) = (x(\varphi, \theta), y(\varphi, \theta), z(\varphi, \theta))$ in Boozer coordinates wraps toroidally and poloidally such that:

3. $x(0,0) \geq x(0,\pi)$,
4. $\frac{\partial z}{\partial \theta}(0,0) \leq 0$,
5. $\frac{\partial y}{\partial \varphi}(0,0) \geq 0$.

These conditions are illustrated in Figure 10. The first two conditions break the freedom about the stellarator symmetric points. The final three conditions ensure that the origin of the surface ($\varphi = 0, \theta = 0$) lies on the outboard side of the stellarator, that the parametrization wraps poloidally clockwise if looking in the $+Y$ direction at the curve given by $\Sigma(\theta, 0)$, and that increasing φ means going counterclockwise about the Z -axis if looking in the $-Z$ direction. If these conditions are not satisfied, we reflect the device about the XY plane, rotate it by a half-period about the Z -axis, or reparametrize the surface so that it wraps in the correct direction. The direction of the inequalities in conditions 1-5 were arbitrarily chosen.

Many quasisymmetric devices are available in the literature optimized for various aspect ratios, with varying quality of quasisymmetry. To plot these devices alongside QUASR ones on the lower dimensional manifold, we determine their feature vectors using the following procedure. First, we take the geometry of the device's outermost surface and use VMEC (Hirshman & Whitson 1983) to determine the vacuum magnetic field on the entire toroidal volume. We take the surface in the equilibrium that has aspect ratio closest to 10 for QA and 12 for QH. The Boozer coordinates on this surface are computed using BOOZ_XFORM (Sanchez *et al.* 2000). Finally, we compute the Fourier harmonics of this surface parametrized in Boozer coordinates. Using this feature vector, $\mathbf{y} \in \mathbb{R}^{663}$, its two-dimensional coordinate projected on the two-dimensional linear manifold is $(\mathbf{d}_1^* \cdot (\mathbf{y} - \boldsymbol{\gamma}^*), \mathbf{d}_2^* \cdot (\mathbf{y} - \boldsymbol{\gamma}^*))$. Devices from the literature are projected onto the principal component plots and labelled. The labels are summarized in Table 2.

Label	n_{fp}	aspect ratio	ι	QS type	Figure #	Reference
BULLER_Op40	2	6.00	0.40 (m)	QA	20	Buller <i>et al.</i> (2024)
GIU_QA	2	6.00	0.42 (m)	QA	20	Giuliani <i>et al.</i> (2022b)
NIES_iota=Op37	2	6.00	0.37 (e)	QA	20	Nies <i>et al.</i> (2024)
NIES_iota=Op42	2	6.00	0.42 (e)	QA	20	Nies <i>et al.</i> (2024)
NIES_AR=10	2	10.0	0.42 (e)	QA	20	Nies <i>et al.</i> (2024)
NIES_AR=8	2	8.00	0.42 (e)	QA	20	Nies <i>et al.</i> (2024)
NIES_AR=6	2	6.00	0.42 (e)	QA	20	Nies <i>et al.</i> (2024)
NIES_AR=4	2	4.00	0.42 (e)	QA	20	Nies <i>et al.</i> (2024)
NIES_AR=2p6	2	2.60	0.42 (e)	QA	20	Nies <i>et al.</i> (2024)
PRECISE_QA	2	6.00	0.42 (m)	QA	20	Landreman & Paul (2022)
BULLER_Op50	2	6.00	0.50 (m)	QA	21	Buller <i>et al.</i> (2024)
BULLER_Op60	2	6.00	0.60 (m)	QA	21	Buller <i>et al.</i> (2024)
NIES_AR=8	3	8.00	0.42 (e)	QA	21	Nies <i>et al.</i> (2024)
NIES_AR=6p5	3	6.50	0.42 (e)	QA	21	Nies <i>et al.</i> (2024)
UNPUBLISHED_NFP3	3	6.00	1.06 (m)	QH	16	Kappel <i>et al.</i> (2024)
NEW_QH	4	13.5	2.29 (m)	QH	14	Rodríguez <i>et al.</i> (2023)
HSX (vacuum)	4	10.0	1.06 (m)	QH	19	Anderson <i>et al.</i> (1995)
WISTELL-A	4	6.72	1.1 (m)	QH	19	Bader <i>et al.</i> (2020)
NIES_AR=3	4	3.00	1.3 (e)	QH	19	Nies <i>et al.</i> (2024)
PRECISE_QH	4	8.00	1.24 (m)	QH	19	Landreman & Paul (2022)

TABLE 2. Labeling of devices from the literature, the figure number on which they appear in this manuscript, along with the value of n_{fp} , type of QS targeted, aspect ratio, and rotational transform. We quote either the mean rotational transform, or the edge rotational transform. These separate cases are highlighted with an ‘m’ or ‘e’ in parentheses.

These devices were all optimized for QS at various aspect ratios, and target rotational transforms. Moreover, some devices were designed to have a target mean rotational transform (Landreman & Paul 2022; Giuliani *et al.* 2022b), while others had a target edge rotational transform (Nies *et al.* 2024). In order to be able to compare them with devices in QUASR, they are projected on the PC plots if they have the same value of n_{fp} , helicity, and mean rotational transform out to aspect ratio 10 (for QA) and 12 (for QH) to an accuracy of ± 0.05 .

Often it is recommended to normalize the data across samples before doing a PCA. One common normalization is to rescale each component of the feature vector to a Gaussian with mean zero and covariance one. The motivation for this is to ensure that none of the features dominates the analysis because its values are much larger than those of the rest of the features. After normalization, each feature makes equally-scaled contributions to the calculation of the covariance matrix. However, this kind of normalization only makes sense if the different components of the feature vector are not meaningfully related to each other and their values have different orders of magnitude because they come from inherently different quantities or phenomena. In our case, the feature vectors contain Fourier coefficients, which decay as the harmonic increases. Therefore, we chose to forgo the normalization of different Fourier components across the devices because the values of the Fourier coefficients have a very important meaning: they are related to each other to compose a single representation.

An alternative approach to visualizing the data set would be to use a vector of Fourier harmonics associated to the coils and their currents. We did not do this due to the inherent non-uniqueness of coil sets, i.e., multiple, vastly different coil sets can produce similar magnetic fields. That being said, we have not fully explored this direction, and it might be interesting to do this in the future.

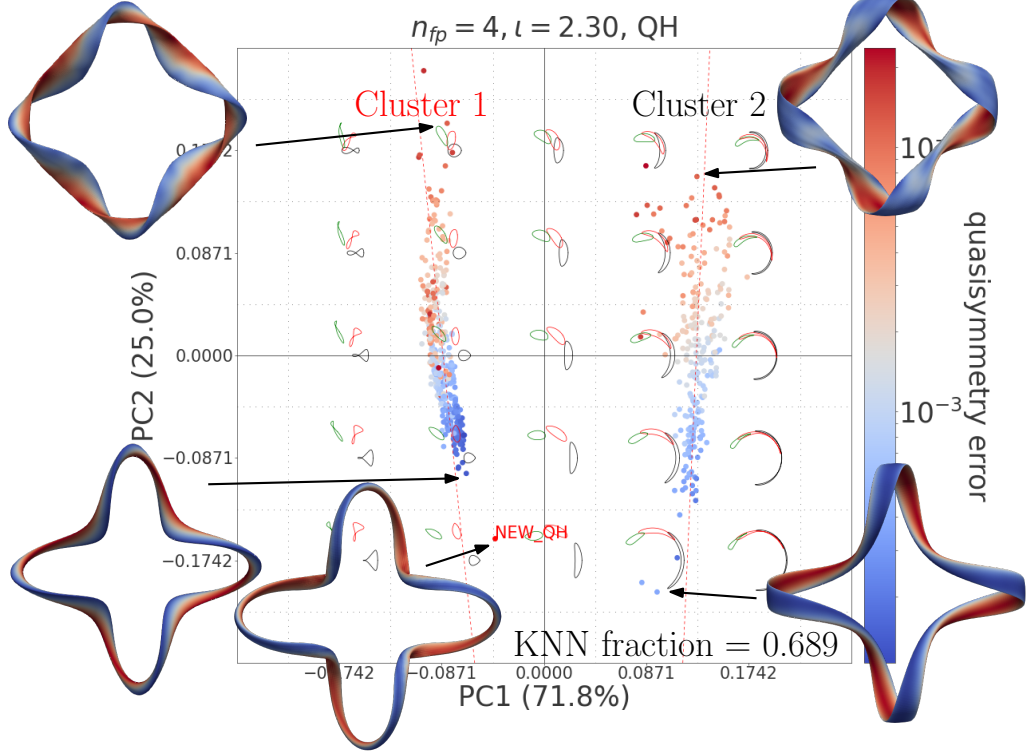


FIGURE 11. PCA of quasihelically symmetric devices in QUASR, along with the new QH device indicated with red text. At the center of each dashed square, we take the associated surface DOFs and generate cross sections to illustrate the geometric diversity of devices. This type of cross section diagram is common in morphometrics literature (Bonhomme *et al.* 2014). The red dashed lines correspond to projections of one-dimensional PCAs of the left and right clusters onto the two-dimensional manifold. The color on the magnetic surfaces corresponds to the local field strength. The quality of quasisymmetry is calculated by taking the square root of the average of (2.1) on a number of surfaces of the equilibrium.

5.2. Quasihelical symmetry ($n_{fp} = 4, \iota = 2.3$)

To start, we look at $n_{fp} = 4$ devices with a mean rotational transform of 2.3 in Figure 11. We observe that there are two distinct clusters of devices. Within these clusters, the devices form a continuum with varying qualities of quasisymmetry.

One may question how faithful this two-dimensional plot is to the true high-dimensional data set. A hint that this plot is an accurate representation of the relationships in the data is the sum of the percentages in the x and y axis labels reveal that a small amount of information is lost in the projection. So, including a third dimension is likely unnecessary to understand how devices relate to each other. Using 10 nearest neighbors in the KNN calculation, the average KNN fraction over all data points is 0.689. This indicates that on average, just under 70% of each node's 10 nearest neighbors in the high-dimensional representation are preserved on the lower dimensional manifold. These projection error measures are comparable to the dimensionality reduction example of data sampled from simple Gaussians, in the introduction of Section 5.

Each point on the landscape plot corresponds to a specific vacuum magnetic field, with associated magnetic surfaces. There are box-shaped regions delineated by dashed lines on the plot. Taking the point at the center of each box, we compute cross sections of

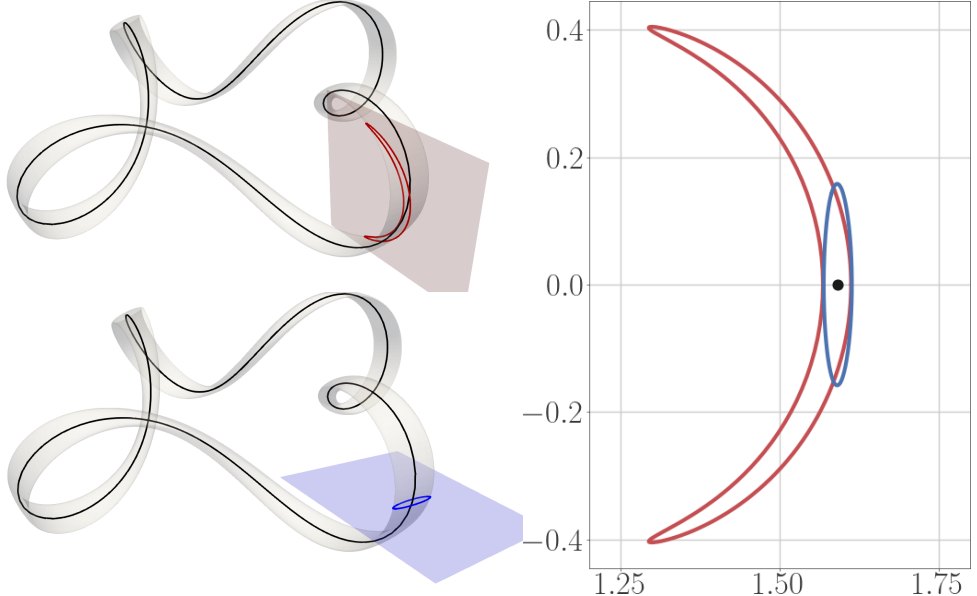


FIGURE 12. Cross sections of a device from cluster 2 in Figure 11. The section is computed in the RZ plane (red) and the plane orthogonal the magnetic axis (blue). The magnetic axis is drawn in black. The cross sections are compared on the rightmost plot. The x , and y -axes correspond to the coordinates of the cross sections on the associated cutting plane. Both planes pass through the same point on the magnetic axis.

the associated magnetic surface. The cross sections are plotted in black, red, and green, associated to the cylindrical angle $\phi = 0, \pi/(2n_{fp}), \pi/n_{fp}$, respectively. This figure makes it clear how devices differ from each other on the plane, and importantly how moving along the principal components affects the geometry of the device. Moving in the positive direction associated to \mathbf{d}_1^* , the elongation appears to increase, while going in the negative direction the elongation decreases. In the positive \mathbf{d}_2^* direction, the relative positions of the cross sections move, and in particular the axis excursion increases. These cross sections do not necessarily correspond to physically relevant devices, as illustrated by the leftmost column, where the cross sections are self-intersecting. This is not surprising, as the devices lie on a nonlinear manifold, and the PCA slices through it with a linear one. If one strays too far away from the origin of the plot (the sample mean), the approximation errors become noticeable and unphysical devices appear.

In optimizing these stellarators, we used a particular surface representation that is compatible with Boozer coordinates, i.e., the surface parametrization is capable of representing surfaces where the two angles on the surface correspond to Boozer coordinates. We find that converting the highly-shaped surfaces, e.g. the device in Figure 12, to a cylindrical representation, as is used in VMEC or DESC, requires more than $m_{\text{pol}}, n_{\text{tor}} = 30$ Fourier modes. If an insufficient number of Fourier modes is used, we observe that the conversion is inaccurate and the surface in cylindrical coordinates presents nonphysical oscillations, an artifact of the imperfect conversion. The number of required Fourier modes for the conversion is substantially more than the number of modes used to design the stellarator ($m_{\text{pol}}, n_{\text{tor}} = 10$) with the representation in equation (5.2)-(5.6). If the device has a large helical excursion of the magnetic axis, cross sections in the RZ plane become highly elongated. This is particularly true for the devices on the right branch, in the bottom quadrant. Another observation about such devices is

that they can generate artificially large cross sections computed in the RZ plane, see the bottom of the rightmost branch in Figure 11. This is illustrated in Figure 12, where we provide cross sections of the device computed in the RZ plane, and the plane orthogonal to the magnetic axis. Comparing the two types of cross section, we see that the one in the plane orthogonal to the axis extends much less in the vertical direction. It would be interesting to explore if these highly shaped devices are attainable using the VMEC, DESC (Panici *et al.* 2023), or GVEC codes (Hindenlang 2019) via optimization.

We also provide the location of the `NEW_QH` device from section 4 and observe again that there are no devices in this subset of QUASR that are close to it. The `NEW_QH` device appears closest to the low elongation branch, in the vicinity of devices with excellent quasisymmetry, but is not contained in QUASR.

Visualizing the continuum of devices in each cluster

We observe that the two clusters appear to lie on separate one-dimensional linear manifolds. Subselecting all the devices in the first cluster where $PC1 < 0$, we do a second PCA on the full feature vector with $D = 663$ entries, and retaining only a single principal component. It appears that the devices are well approximated by a one-dimensional linear manifold, because $\lambda_1/(\lambda_1 + \dots + \lambda_{663}) = 0.916$. The same thing can be done for devices in the second cluster, i.e. where $PC1 > 0$. Again, the devices here are well approximated by a one-dimensional linear manifold because $\lambda_1/(\lambda_1 + \dots + \lambda_{663}) = 0.876$. After these separate one-dimensional PCAs, each device from the first cluster now has a single coordinate called PC, which lies on the interval $[\min(PC), \max(PC)]$. We can easily visualize the progression of the device geometries along these one-dimensional manifold by sampling devices uniformly according to the principal component label, i.e., devices with a principal component label that is approximately $\min(PC1) + i(\max(PC) - \min(PC))/N$ for $i = 0, \dots, N$. In Figure 11, we have projected these one-dimensional manifolds onto the plane, indicated by two red dashed lines. The progression of devices along these lines in both clusters is shown in Figure 13, where the transition between the endpoint geometries appears smooth. This is evidence that the devices in each cluster in the full $D = 663$ dimensional feature space lie on simple one-dimensional continua.

The difference between the two clusters can in this way also be made clearer. We said before that \mathbf{d}_1^* appeared to control the elongation of cross sections, with cluster 2 characterized by an increased value for it. However, from Figure 13, there is a key geometric difference between the clusters that explains this observation and which has to do with the difference in twisting of the devices. At the sharpest corners in the RZ projection, cluster 1 devices have a magnetic axis mainly lying on the plane, while cluster 2 devices have their axes coming off the plane. This difference in bending and twisting is key in controlling rotational transform and other properties, and is worth further exploration in the future.

5.3. Quasihelical symmetry ($n_{fp} = 3, \iota = 1.1$)

In Figure 14, we plot the landscape of devices for a lower rotational transform $\iota = 1.1$ and $n_{fp} = 3$, where it appears that little information was lost in the projection. We find the devices in QUASR here are close to an unpublished device from (Kappel *et al.* 2024). The KNN fraction is quite high, 0.794. In contrast to the previous PCA, both principal components appear to modify the devices' elongation and the positioning of the cross sections. We note that here, there does not appear to be two separate clusters of devices and the devices form a V-shaped continuum.

To parameterize this one-dimensional continuum, a PCA is inappropriate here as clearly the manifold is nonlinear. Instead, we use the isomap algorithm (Tenenbaum

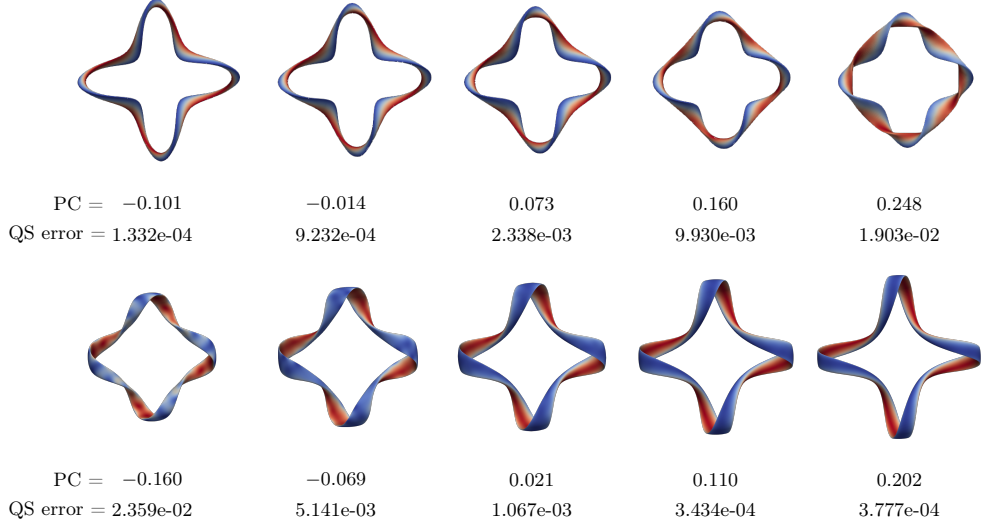


FIGURE 13. Continuum of devices in QUASAR. The first and second row correspond to the left and right cluster in Figure 11, respectively. The numbers below these devices are their corresponding principal component values, and quasisymmetry errors. The color on the magnetic surfaces corresponds to the local field strength.

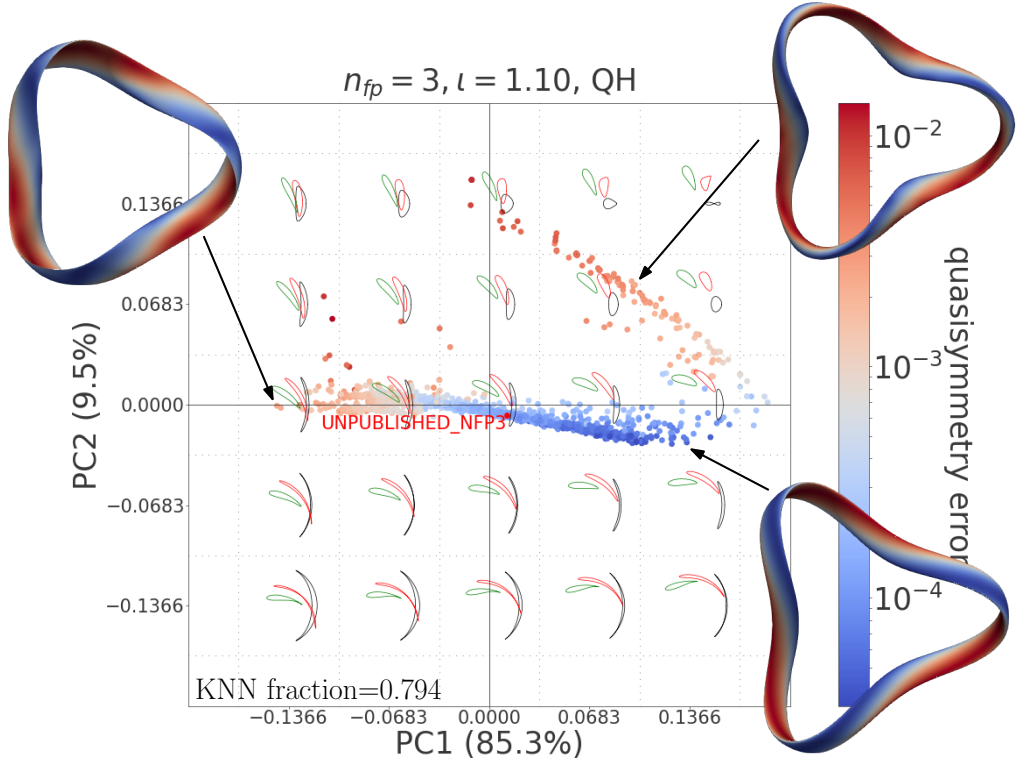


FIGURE 14. PCA of quasihelically symmetric devices in QUASAR, along with an unpublished device from (Kappel *et al.* 2024), indicated with red text. The color on the magnetic surfaces corresponds to the local field strength.

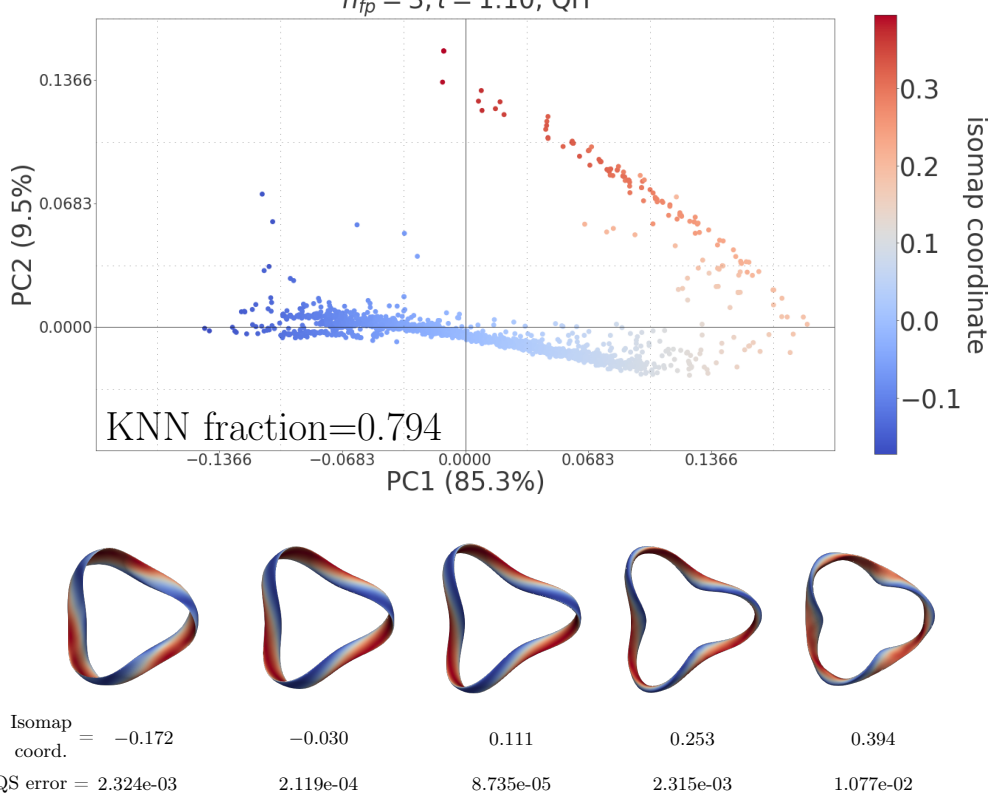


FIGURE 15. The nonlinear manifold in Figure 14 can be parametrized with a single coordinate using the isomap algorithm. The bottom row of devices are uniformly sampled from the isomap embedding, and the numbers below these devices corresponds to the isomap coordinate and the quality of quasisymmetry.

et al. 2000) to visualize the progression of the device geometries along the manifold. The isomap algorithm works by generating a connectivity graph between data points using the k -nearest neighbors of each node. Then, pairwise distances between points are computed by traversing the connectivity graph. The multidimensional scaling algorithm (Kruskal 1964) attempts to find a lower dimensional representation that preserves these pairwise distances. Our aim is to find a one-dimensional labelling of the devices so that the devices can be ordered, similar to Section 5.2. Applying the isomap algorithm on the full $D = 663$ dimensional data points, we obtain the embedding shown in Figure 15, i.e., each device is given a one-dimensional coordinate. Uniformly sampling this coordinate, the progression of devices in the bottom row of the figure is obtained.

5.4. Quasihelical symmetry ($n_{fp} = 5, \iota = 2.5$)

In this section, we plot the two-dimensional landscape of devices with a rotational transform $\iota = 2.50$ and $n_{fp} = 5$ in Figure 16, where it appears that a third dimension might have provided a more faithful representation of the data. The first principal component appears to shift the relative positions of the cross sections, while the second principal component appears to act on the elongation of the device (similarly to the $n_{fp} = 4$ before). There appears to be two separate clusters of devices, where the second cluster contains the most quasisymmetric devices (again there seems to be a parallel

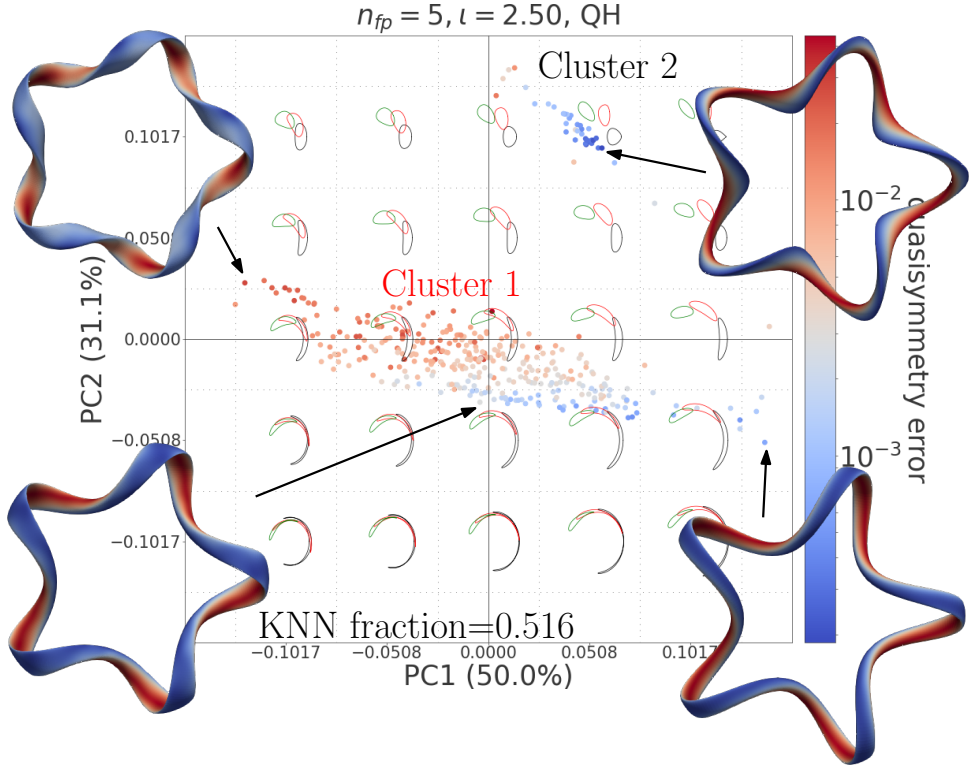


FIGURE 16. PCA of quasihelically symmetric devices in QUASR when $\iota = 2.5$ and $n_{fp} = 5$. Two clusters are labeled and devices from them are plotted. The color on the magnetic surfaces corresponds to the local field strength.

to the $n_{fp} = 4$ scenario, even on the geometric behavior within and between clusters). A non-negligible amount of information was lost in this projection, as the sum of the PC ratios is just over 80%. Similarly, the KNN fraction is just over 0.50. To provide a more accurate representation of the data, we augment Figure 16 with a third principal component in Figure 17. Two-dimensional projections of the data on the PC1-PC2, PC1-PC3, and PC2-PC3 planes are also provided to make the three-dimensional nature of the data more easily understood. Our projection error measures immediately improve as the sum of the PC ratios is approximately 90%, and the KNN fraction increases to 0.702.

We note that the dimensionality of the clusters appears different, which can be observed in two-dimensional projections of Figure 17: the first cluster is a three-dimensional cloud, while the second cluster appears to have very little variation in the third PC. The higher dimensionality of cluster 1 can be quantified by observing the cumulative PC ratio as the number of principal components used to represent cluster 1 and 2 on the left of Figure 17. It takes three PCs for the cumulative PC ratio of cluster 1 to pass 0.9, while it takes only two for cluster 2.

Further evidence that the data set comprises clusters is provided in Figure 18, which is a histogram of pairwise Euclidean distances between the devices of Figure 11, 14, 16. We find that the histogram in Figure 18a and Figure 18c are both clearly bimodal. Moreover, the histograms of pairwise distances within the clusters are unimodal.

Figure 18b reveals that these pairwise distance histogram plots do not always tell the

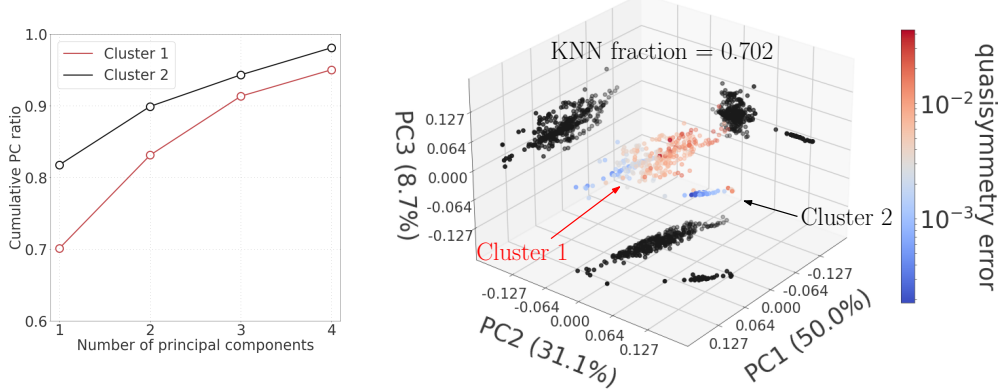


FIGURE 17. On the left, the cumulative PC ratio with increasing number of principal components used to represent the two clusters from Figure 16. On the right, PCA of quasihelically symmetric devices in QUASAR when $\iota = 2.5$ and $n_{fp} = 5$, similar to Figure 16 but with a third principal component. Two-dimensional projections of the data on the PC1-PC2, PC1-PC3, and PC2-PC3 planes are also provided in black to make the three-dimensional nature of the data more easily understood.

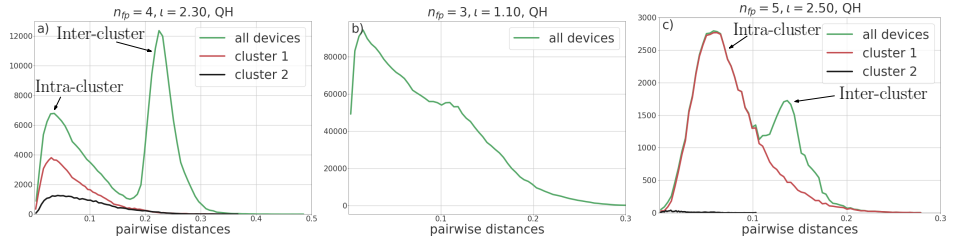


FIGURE 18. Histogram of pairwise distances for all devices, or clusters 1 and 2 in Figure 11, 14, and 16, respectively.

whole story. This plot appears to have one clear peak, with another that is difficult to make out. From this plot, one might conclude that there are possibly two clusters, though the V-shaped structure of the data in Figure 16 can somewhat explain the histogram shape.

5.5. Quasihelical symmetry ($n_{fp} = 4, \iota = 1.1, 1.2$)

We look at another region of the QH design space that have been explored in the literature. When $n_{fp} = 4$ and $\iota = 1.1, 1.2$ in Figure 19. On both plots, there are two clusters corresponding to devices with $\iota = 1.1$ and another when $\iota = 1.2$. The HSX, WISTELL-A, PRECISE_QH devices are located on the main clusters. There is a separate agglomeration of devices away from the main clusters with arguably comparable quality of quasimmetry. Combining devices with two separate values of ι does not appear to significantly degrade the two-dimensional visualization of the data, as the sum of the PC ratios exceeds 90%, and the KNN fraction is 0.672.

5.6. Quasimmetry

In Figure 20, we complete a PCA on quasimmetric devices in QUASAR with $n_{fp} = 2$ and $\iota = 0.4$. The cumulative PC ratio is just over 80%, revealing that a non-negligible amount of information is lost in this projection, and it might be useful to include a third principal component in the visualization. Given the two principal axes, we project devices

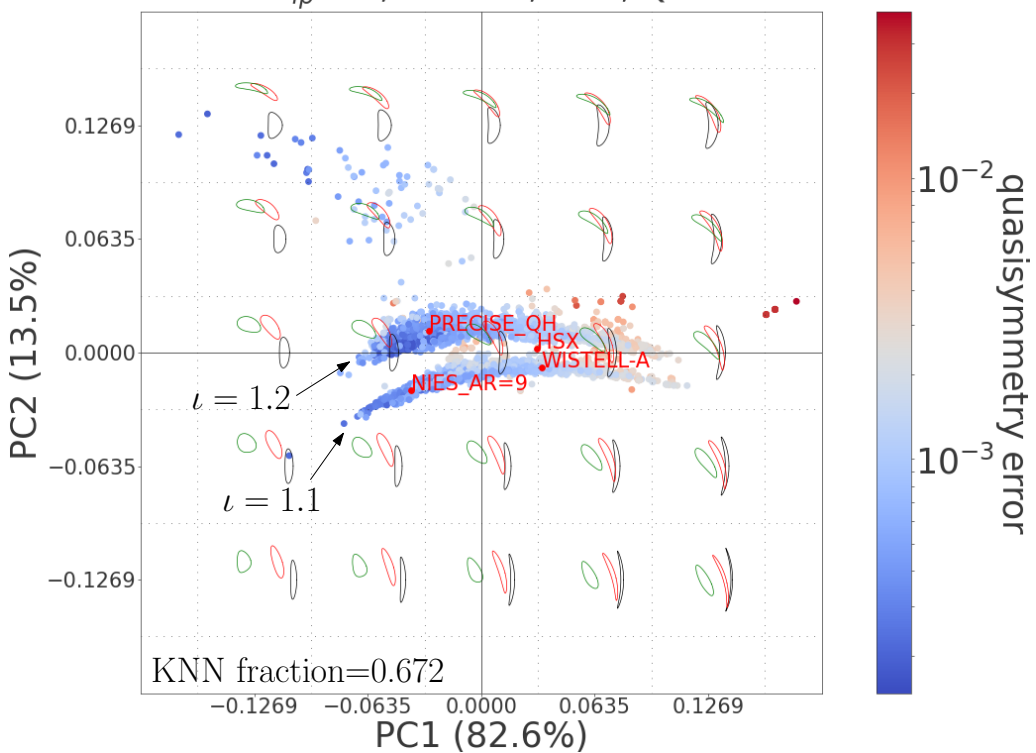


FIGURE 19. PCA of quasihelically symmetric devices in QUASR when $\iota = 1.1, 1.2$ and $n_{fp} = 4$. There are two main clusters associated to devices with $\iota = 1.1, 1.2$ labeled on the plot.

outside QUASR onto the figure and label them. This area of the parameter space is well explored. In Figure 21, we do a PCA for QA devices, subselected based on their rotational transform ($\iota = 0.5, 0.6$) and number of field periods ($n_{fp} = 2, 3$). Labeled devices from the literature appear similar to the devices in QUASR. We do not provide cross sections of hypothetical devices on the linear manifold as we did in previous sections because, visually, the cross sections do not differ significantly from each other.

The analysis from section 4 reveals that the region of QA devices with favorable quasisymmetry is small, and moreover it shrinks with increasing shaping of the device. This bears out in the PCA analysis here too, as we find that there is not much geometric diversity of the devices at the aspect ratio studied. Notably, the Landreman-Paul QA device (PRECISE_QA) is close on the plane to the device called GIU_QA. This device was obtained by providing the PRECISE_QA device as an initial guess to a direct coil optimization algorithm. The quality of quasisymmetry in these two devices differs by almost an order of magnitude, despite the geometrical proximity on the plot.

6. Discussion and conclusion

The main goal of this paper was to introduce a new data set of optimized stellarators, and provide tools to navigate the contents of it. We highlight a few devices in QUASR and give some physics analysis of them. Then, a quasisymmetry landscape is constructed, and it is determined where the stellarators QUASR fall on it. We find close correspondence of devices in QUASR to regions of favorable near-axis quasisymmetry. This approach

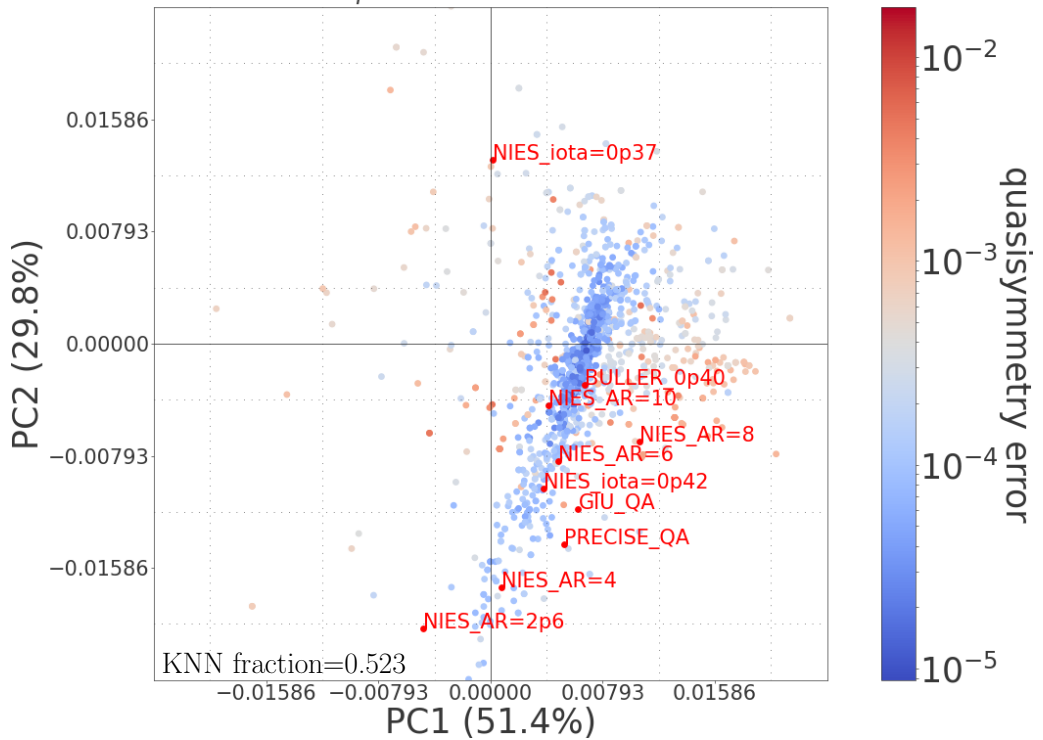
$n_{fp} = 2, \iota = 0.40, \text{QA}$


FIGURE 20. PCA of quasaxisymmetric devices in QUASR along with devices in the literature, indicated with red text.

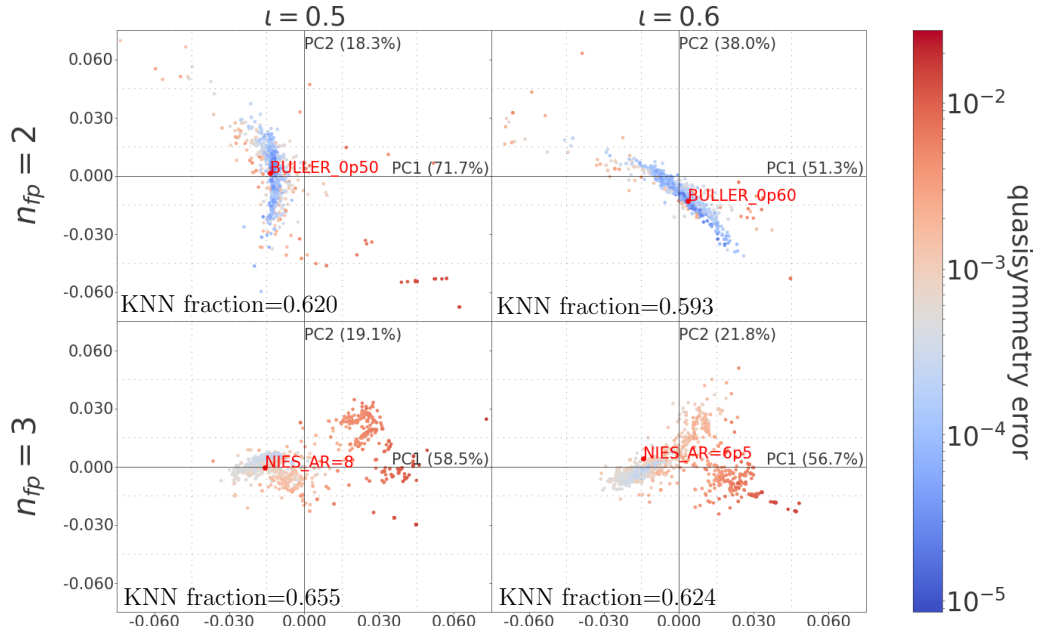


FIGURE 21. PCA of quasaxisymmetric devices in QUASR along with devices in the literature, indicated with red text.

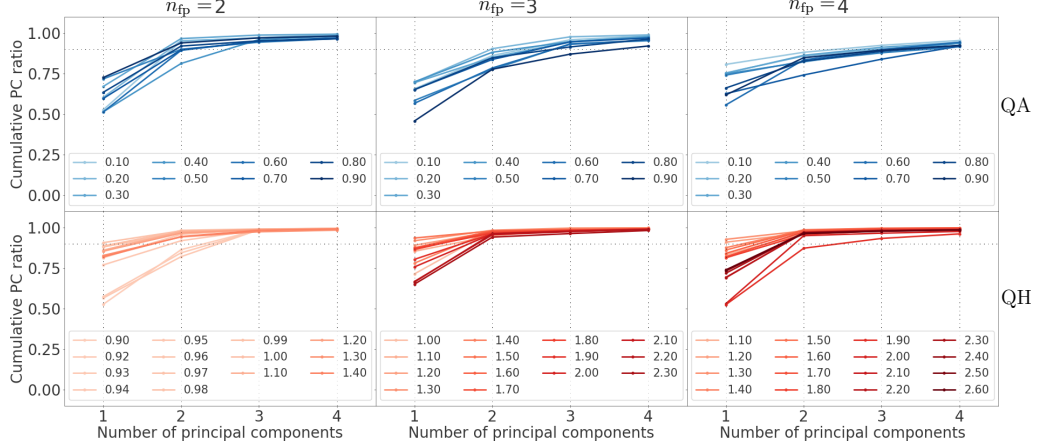


FIGURE 22. The cumulative PC ratio of subsets of the data for various combinations of n_{fp} , ι and helicity. The first and second rows correspond to QA and QH devices, respectively. The columns correspond to particular values of n_{fp} , and the curves correspond to different values of ι . The horizontal dashed line corresponds to a cumulative PC ratio of 0.9.

does not apply to the full set of devices in QUASR, so we proceed to a PCA for a more complete analysis. On the subsets of the data set that we have explored in this work, we find that the first and second principal components act predominantly on the elongation (and different field twisting), and relative positions of cross sections of the magnetic surfaces. For some subsets of the data, we observe clear clusters. Within the clusters, we find evidence that the devices form a continuum.

PCA is not only a very useful dimensionality reduction and visualization tool, it can also be used to create compact representations of the data that can be used for initial stages of optimization. We find that for many subsets of the data, little information is lost when using two to three principal components, and it is possible to attain a cumulative PC ratio of 0.9. This is illustrated in Figure 22, where we compute a PCA for various combinations of n_{fp} and ι for QA and QH devices. This illustrates that much of the variation between the devices can be characterized on a low-dimensional, linear manifold. This is useful because very simple, linear formulas can be used to generate warm starts for optimization. Alternatively, one might attempt optimizing in the PC subspace. These directions are not explored in this paper.

7. Data availability

The latest version of the QUASR data set can be found at <https://zenodo.org/doi/10.5281/zenodo.10050655>. It can be visually explored at quasr.flatironinstitute.org.

8. Acknowledgements

The authors would like to thank Flatiron's Scientific Computing Core (SCC). We would also like to thank Marsha Berger, Rogerio Jorge, Matt Landreman, Elizabeth Paul, Manas Rachh, and Lawrence Saul for helpful discussions. E. R. was supported by a grant of the Alexander-von-Humboldt-Stiftung, Bonn, Germany, through a postdoctoral research fellowship.

REFERENCES

ANDERSON, F. S. B., ALMAGRI, A. F., ANDERSON, D. T., MATTHEWS, P. G., TALMADGE, J. N. & SHOHET, J. L. 1995 The helically symmetric experiment, (HSX) goals, design and status. *Fusion Technology* **27** (3T), 273–277.

BADER, A., FABER, B. J., SCHMITT, J. C., ANDERSON, D. T., DREVLAK, M., DUFF, J. M., FRERICHS, H., HEGNA, C.C., KRUGER, T.G., LANDREMAN, M. & OTHERS 2020 Advancing the physics basis for quasi-helically symmetric stellarators. *Journal of Plasma Physics* **86** (5), 905860506.

BISHOP, C. 2006 *Pattern Recognition and Machine Learning*. Springer.

BLANK, HJ DE 2004 Guiding center motion. *Fusion science and technology* **45** (2T), 47–54.

BONHOMME, V., PICQ, S., GAUCHEREL, C. & CLAUDE, J. 2014 Momocs: outline analysis using R. *Journal of Statistical Software* **56**, 1–24.

BOOZER, A. H 1981a Plasma equilibrium with rational magnetic surfaces. *Tech. Rep.* Princeton Univ.

BOOZER, A. H. 1981b Transport and isomorphic equilibria. *Tech. Rep.* Princeton Plasma Physics Lab.(PPPL), Princeton, NJ (United States).

BULLER, S., LANDREMAN, M., KAPPEL, J. & GAUR, R. 2024 A family of quasi-axisymmetric stellarators with varied rotational transform. ArXiv:2401.09021 [physics].

BURBY, J. W., KALLINIKOS, N. & MACKAY, R. S 2020 Some mathematics for quasi-symmetry. *Journal of Mathematical Physics* **61** (9).

ERIKSSON, D., PEARCE, M., GARDNER, J., TURNER, R. D. & POLOCZEK, M. 2019 Scalable global optimization via local Bayesian optimization. In *Advances in Neural Information Processing Systems*, pp. 5496–5507.

FULLER JR, E. J. 1999 *The geometric and topological structure of holonomic knots*. University of Georgia.

GARREN, D. A. & BOOZER, A. H. 1991 Existence of quasihelically symmetric stellarators. *Physics of Fluids B* **3** (10), 2822–2834.

GIULIANI, A. 2024 Direct stellarator coil design using global optimization: application to a comprehensive exploration of quasi-axisymmetric devices. *Journal of Plasma Physics* **90** (3), 905900303.

GIULIANI, A., WECHSUNG, F., CERFON, A., LANDREMAN, M. & STADLER, G. 2023 Direct stellarator coil optimization for nested magnetic surfaces with precise quasi-symmetry. *Physics of Plasmas* **30** (4), 042511, arXiv: https://pubs.aip.org/aip/pop/article-pdf/doi/10.1063/5.0129716/16831861/042511_1_5.0129716.pdf.

GIULIANI, A., WECHSUNG, F., CERFON, A., STADLER, G. & LANDREMAN, M. 2022a Single-stage gradient-based stellarator coil design: Optimization for near-axis quasi-symmetry. *Journal of Computational Physics* **459**, 111147.

GIULIANI, A., WECHSUNG, F., STADLER, G., CERFON, A. & LANDREMAN, M. 2022b Direct computation of magnetic surfaces in Boozer coordinates and coil optimization for quasisymmetry. *Journal of Plasma Physics* **88** (4), 905880401.

HELANDER, P. 2014 Theory of plasma confinement in non-axisymmetric magnetic fields. *Reports on Progress in Physics* **77** (8), 087001.

HINDENLANG, F. 2019 A newly developed 3d ideal mhd galerkin variational equilibrium code.

HIRSHMAN, S. P. & WHITSON, J. P 1983 Steepest-descent moment method for three-dimensional magnetohydrodynamic equilibria. *PF* **26** (12), 3553.

JOLLIFFE, I. T. 1990 Principal component analysis: a beginner's guide—i. introduction and application. *Weather* **45** (10), 375–382.

JORGE, R., GIULIANI, A. & LOIZU, J. 2024 Simplified and flexible coils for stellarators using single-stage optimization, arXiv: 2406.07830.

KAPPEL, J., LANDREMAN, M. & MALHOTRA, D. 2024 The magnetic gradient scale length explains why certain plasmas require close external magnetic coils. *Plasma Physics and Controlled Fusion* **66** (2), 025018.

KOBAK, D. & BERENS, P. 2019 The art of using t-sne for single-cell transcriptomics. *Nature communications* **10** (1), 5416.

KRUSKAL, J. B. 1964 Nonmetric multidimensional scaling: a numerical method. *Psychometrika* **29** (2), 115–129.

LANDREMAN, M. 2019 Optimized quasisymmetric stellarators are consistent with the Garren-Boozer construction. *Plasma Physics and Controlled Fusion* **61** (7), 075001.

LANDREMAN, M. 2022 Mapping the space of quasisymmetric stellarators using optimized near-axis expansion. *Journal of Plasma Physics* **88** (6), 905880616.

LANDREMAN, M., JORGE, R., RODRIGUEZ, E. & DUDT, D. 2024 *landreman/pyQSC*.

LANDREMAN, M., MEDASANI, B., WECHSUNG, F., GIULIANI, A., JORGE, R. & ZHU, C. 2021 Simsopt: a flexible framework for stellarator optimization. *Journal of Open Source Software* **6** (65), 3525.

LANDREMAN, M. & PAUL, E. 2022 Magnetic fields with precise quasisymmetry for plasma confinement. *Phys. Rev. Lett.* **128**, 035001.

LANDREMAN, M. & SENGUPTA, W. 2019a Constructing stellarators with quasisymmetry to high order. *Journal of Plasma Physics* **85** (6), 815850601.

LANDREMAN, M. & SENGUPTA, W. 2019b Constructing stellarators with quasisymmetry to high order. *Journal of Plasma Physics* **85** (6), 815850601.

LANDREMAN, M., SENGUPTA, W. & PLUNK, G. G. 2019 Direct construction of optimized stellarator shapes. part 2. numerical quasisymmetric solutions. *Journal of Plasma Physics* **85** (1), 905850103.

LEE, J. A. & VERLEYSEN, M. 2009 Quality assessment of dimensionality reduction: Rank-based criteria. *Neurocomputing* **72** (7-9), 1431–1443.

VAN DER MAATEN, L. & HINTON, G. 2008 Visualizing data using t-sne. *Journal of machine learning research* **9** (11).

MOFFATT, H. K. & RICCA, R. L. 1992 Helicity and the călugăreanu invariant. *Proceedings of the Royal Society of London. Series A: Mathematical and Physical Sciences* **439** (1906), 411–429.

NAJMABADI, F., RAFFRAY, A. R., ABDEL-KHALIK, S. I., BROMBERG, L., CROSATTI, L., EL-GUEBALY, L., GARABEDIAN, P. R., GROSSMAN, A. A., HENDERSON, D., IBRAHIM, A. & OTHERS 2008 The ARIES-CS compact stellarator fusion power plant. *Fusion Science and Technology* **54** (3), 655–672.

NIES, R., PAUL, E. J., PANICI, D., HUDSON, S. R. & BHATTACHARJEE, A. 2024 Exploration of the parameter space of quasisymmetric stellarator vacuum fields through adjoint optimisation. *arXiv preprint arXiv:2404.02240*.

NÜHRENBERG, J. & ZILLE, R. 1988 Quasi-helically symmetric toroidal stellarators. *Physics Letters A* **129** (2), 113–117.

OBERTI, C. & RICCA, R. L. 2016 On torus knots and unknots. *Journal of Knot Theory and Its Ramifications* **25** (06), 1650036.

PANICI, D., CONLIN, R., DUDT, D.W., UNALMIS, K. & KOLEMEN, E. 2023 The desc stellarator code suite. part 1. quick and accurate equilibria computations. *Journal of Plasma Physics* **89** (3), 955890303.

PAUL, E. J., BHATTACHARJEE, A., LANDREMAN, M., ALEX, D., VELASCO, J. L. & NIES, R. 2022 Energetic particle loss mechanisms in reactor-scale equilibria close to quasisymmetry. *Nuclear Fusion* **62** (12), 126054.

RODRIGUEZ, E., HELANDER, P. & BHATTACHARJEE, A. 2020 Necessary and sufficient conditions for quasisymmetry. *Physics of Plasmas* **27** (6).

RODRIGUEZ, E., PAUL, E. J. & BHATTACHARJEE, A. 2022a Measures of quasisymmetry for stellarators. *Journal of Plasma Physics* **88** (1), 905880109.

RODRIGUEZ, E., SENGUPTA, W. & BHATTACHARJEE, A. 2022b Phases and phase-transitions in quasisymmetric configuration space. *Plasma Physics and Controlled Fusion* **64** (10), 105006.

RODRÍGUEZ, E., SENGUPTA, W. & BHATTACHARJEE, A. 2023 Constructing the space of quasisymmetric stellarators through near-axis expansion. *Plasma Physics and Controlled Fusion* **65** (9), 095004.

SANCHEZ, R., HIRSHMAN, S. P., WARE, A. S., BERRY, L. A. & SPONG, D. A. 2000 Ballooning stability optimization of low-aspect-ratio stellarators. *Plasma physics and controlled fusion* **42** (6), 641.

SPITZER, L. 1958 The stellarator concept. *Physics of Fluids* **1** (4), 253.

TENENBAUM, J. B., SILVA, V. DE & LANGFORD, J. C. 2000 A global geometric framework for nonlinear dimensionality reduction. *science* **290** (5500), 2319–2323.

TREFETHEN, L. N & WEIDEMAN, J. A. C. 2014 The exponentially convergent trapezoidal rule. *SIAM review* **56** (3), 385–458.

WECHSUNG, F., LANDREMAN, M., GIULIANI, A., CERFON, A. & STADLER, G. 2022 Precise stellarator quasi-symmetry can be achieved with electromagnetic coils. *Proceedings of the National Academy of Sciences* **119** (13), e2202084119.